

Scatterometry Using Speckle Correlations

*Submitted in partial fulfillment of the requirements for
the degree of*

Doctor of Philosophy

in

Electrical and Computer Engineering

Bakari Hassan

B.S., Applied Physics, Morehouse College

B.S., Aerospace Engineering, University of Michigan

M.S., Electrical Engineering and Computer Science, University of California Los Angeles

Carnegie Mellon University

Pittsburgh, Pennsylvania

December 2024

© Bakari Hassan, 2024

All Rights Reserved

Abstract

Material acquisition describes the process of inferring properties of materials from observations. We are interested in acquiring a scattering property of materials called the scattering phase function which governs the spherical directionality of scattered light intensity. The phase function largely influences the translucent appearance of materials and is driven by material properties such as the type and size of particles in the medium, so it is essential for characterization.

One approach relies on reducing sample optical density such that light paths through the material are scattered once on average. The phase function is then inferred from the relative scattered intensities in different directions. However, this method is limited to classes of materials that can be sliced thinly or diluted. An alternative approach estimates the scattering phase function by inverting the radiative transfer equation. Although it does not require isolating single-scattering events, it is costly and relies on good initialization due to its use of stochastic gradient descent. Efficient, closed-form approaches that rely on the memory effect have been developed for material acquisition from thick samples. By illuminating a sample with coherent laser light and capturing speckle patterns, correlations within the memory effect range allow the single-scattered component to be measured in the presence of high-order scattering. However, the proposed acquisition system measures the scattering phase function over a small angular range of a few degrees due to inherent angular limits of a 4f system.

In this work, we detail material acquisition over angular ranges approaching 180° via scatterometry. Our approach is similar to reflectometry wherein we use two sources fixed to a goniometer that rotates around a sample. We use two mutually coherent laser beams separated by a small angle to maximize speckle correlation. Their respective speckle patterns are acquired using a camera, and the phase function in the mean direction of the two laser beams is proportional to the speckle correlation. The goniometer then rotates the illuminators about the sample to measure the scattering phase function over a large range without the angular limitations inherent in 4f imaging systems. Our results are relevant to graphics applications such as photorealistic augmented reality as well as areas outside graphics and vision such as non-invasive medical diagnostics, remote sensing, and particle sizing for quality assurance.

Contents

List of Figures	viii
List of Tables	xii
1 Introduction	1
1.0.1 Thesis contributions	2
1.1 Material acquisition (related work)	2
1.2 Background	4
1.2.1 Scattering material representation	4
1.2.2 Phase function from speckle images	5
1.3 Thesis contributions	5
2 Speckle Correlation	7
3 Scatterometer Design	9
3.1 System design	9
3.1.1 Illumination	11
3.1.2 Reference Camera	11
3.1.3 Acquisition camera	11
3.1.4 Acquisition camera modifications	12
3.1.5 Camera mount	13
3.1.6 Illuminator Motion assembly	14
3.1.7 Natural Bending Frequency	18
3.1.8 Collimator Mount	22
3.1.9 Sample assembly	23
3.1.10 Illumination polarization control	23

3.2	Sample Analysis Station	25
4	Scatterometer Calibration and Alignment	27
4.1	Calibration and alignment	27
4.2	Calibration Targets	27
4.3	Lower Stage Calibration	28
4.3.1	Stage Position & Beam Direction as a Function of θ	29
4.3.2	Azimuth Stage Location	30
4.3.3	Ray Envelope Center	31
4.3.4	Ray Envelope Isoline	32
4.3.5	Training & Validation Datasets	32
4.4	Sample Motion Assembly Calibration	33
4.5	Aligning Sample and Illuminator Assemblies	33
4.5.1	Rotation	33
4.6	Aligning Calibration Target with Sample Motion Assembly Rotation Axis	34
4.7	Aligning Sample Motion Assembly and Illumination Beams	35
4.8	Aligning Calibration Target with Illumination Beams	37
4.9	Note: Proposal:Acquisition Camera Calibration	37
4.9.1	Intrinsics	39
4.9.2	Extrinsics & Lens Distortion	39
4.9.3	Validation	39
4.10	Note: Proposal:Illuminator Assembly Calibration	40
4.10.1	Note: Proposal:Stage Position & Beam Direction as a Function of θ	41
4.11	Acquisition Camera Calibration	41
4.11.1	Beam Calibration	42
4.12	Note: Proposal:Acquisition Light Efficiency	42
4.13	Note: Proposal:Expected Results	45
5	Scattering Sample Preparation	49
5.0.1	Equipment	49
5.0.2	Procedure	50
5.0.3	Sample Characterization	51
6	Acquisition	53

6.1	Scattering Samples	53
6.2	Acquisition	53
6.3	Maximizing Light Scattered Towards Camera	53
6.3.1	Optimizing Illumination & Sample Orientation to Maximize Light Transmission .	53
6.3.2	Simulation	57
6.3.3	Depolarizer Spatial Characterization	57
6.3.4	Data Processing	59
7	Appendices	61
7.1	Calibration Target Design	61
7.2	Reference Camera Lens Selection	62
7.3	Sample Preparation	62
7.4	Ziegler-Nichols Tuning Method	64
7.5	Parts Lists	65
7.6	Thin lens model validation: macro lenses	65
7.7	Technical drawings	65
8	Technical Drawings	73
8.1	5 Series 20 hole - cross flat plate (P/N 4233-m)	74
Bibliography		75

List of Figures

1	Introduction	1
2	Speckle Correlation	7
3	Scatterometer Design	9
3.1	(a) Laboratory scatterometer setup; (b) CAD rendering of speckle correlation scatterometer .	10
3.2	Light path diagram for speckle correlation scatterometer	10
3.3	(a); (b)	11
3.4	13
3.5	(a); (b);	14
3.6	TODO: Replace with updated figure, add subfigure labels;	18
3.7	Aluminum extrusion profiles in order of increasing aspect ratio. All dimensions are in inches. TODO: ADD REINSERT CROSS-SECTION LABELS.	21
3.8	(a); (b)	21
3.9	(a) Maximum beam bending and torsional deflection due to the illuminator assembly TODO: RERUN TORSIONAL ANALYSIS WITH UPDATED PARAMETERS; (b) Natural beam bending frequency due to the illuminator assembly	22
3.10	(a) CAD front view of collimator mount; (b) CAD side view showing the relative orientations of illumination beams; (c) CAD perspective view; (d) Fully assembled collimator mount which controls vertical and angular illuminator separation. Beam diameter is also controlled using motorized iris diaphragms.; TODO: Replace single collage with subfigures.	23

3.11	(a) Sample motion assembly without sample mount; (b) Sample mount configured for calibration target (not drawn to scale with respect to (a)); (c) Sample mount configured for scattering sample on a microscope slide (not drawn to scale with respect to (a)); (d) Sample mount shown on top of sample assembly with calibration target installed	24
3.12	25
3.13	CAD rendering of the sample analysis station	26
4	Scatterometer Calibration and Alignment	27
4.1	a: Speckle correlation computation pipeline. The sample is illuminated by two beams, and the correlation is computed using a differential sensor. b: Physical setup with sample placed on the circular breadboard. The illumination stand rotates about the sample while the sensing stand measures scattered light. The differential photodetector enables fast correlation computation. c: Geometry used to develop forward model for inverse problem estimation of 3D beam-plane intersection points. d: Mean estimation errors for training and validation phases showing angular dependence of error.	28
4.2	Perpendicular offsets of the four observed beam-plane intersections with respect to the estimated beam direction. Each plot is for an azimuthal angle $\theta \in \Theta$. The cause of increasing perpendicular offsets for increasing angle with respect to the plane normal and anti-normal is unknown.	29
4.3	RT-5 Geometry - Frustrum top Surface	30
4.4	Sample motion assembly without sample mount	35
4.5	Combined figure	36
4.6	36
4.7	38
4.8	Top: Target and beam misaligned due to non-zero angle between the beam and the target normal; Bottom: d aligned with normal vector n . Note: Update by replacing d with kbar.	38
4.9	Left: Composite of 11 images of both illuminators spanning an azimuth range 3.5° . Right: The acquisition camera's focal length is the constant of proportionality of image point displacement and the tangent of the internal ray angle with respect to the optical axis.	39
4.10	Ray envelope defined as the locus of points of closest encounter between the illumination beam and its rotation axis	41

4.11 (a) The acquisition camera's focal length is the constant of proportionality of image point displacement and the tangent of the internal ray angle with respect to the optical axis; (b) Composite of 11 images of both illuminators spanning an azimuth range 3.5° ; (c) Reprojection error as a function of principal point shifts along the y-axis and external pitch rotation is not strictly convex, showing the numerical ambiguity of principal point shifting and camera rotation. This ambiguity holds for the x-axis and panning as well.	43
4.12 Left: Optimal sample rotation stage position and linear polarization angle as a function of azimuthal illumination angle. The linear polarization angle schedule contains discontinuities in the range $(-50^\circ, 50^\circ)$ due to rounding errors; Right: Comparison of light transmitted towards camera when choosing the optimal sample orientation versus a static sample shows an approximate 15% increase on average.	46
4.13 Speckle images of $10\mu\text{m}$ monodisperse SiO_2 beads acquired using scatterometer setup. Left: Top illuminator activated; Center: Both illuminators activated; Right: Bottom illuminator activated	46
4.14 An expected result is acquiring the scattering phase function for a larger range of scattering angles than the literature.	47
5 Scattering Sample Preparation	49
6 Acquisition	53
6.1	57
6.2	58
6.3	59
7 Appendices	61
7.1 Top row: Original target used for calibration caused irregular beam spot shapes which produced noisy centroids. Bottom row: Windowed target used now to avoid albedo issues when imaging beam spots.	61
8 Technical Drawings	73

List of Tables

3.1	Illumination Configurations	10
3.2	Acquisition camera specifications	12
3.3	Cross-sectional & material properties of aluminum extrusions [21]	20
3.4	Physical paraemters for structural analysis assuming 12 deg/s azimuthal stage angular rate with 300 ms deceleration duration.	20
7.1	Ziegler-Nichols method	65
7.2	Parts List - Scatterometer Support Equipment	66
7.3	Parts List - Laser Path	67
7.4	Parts List - Illuminator Motion Assembly	68
7.5	Parts List - Counterweight	69
7.6	Parts List - Sample Motion Assembly	69
7.7	Parts List - Acquisition Camera Assembly	70
7.8	Parts List - Sample Analysis Station	71
7.9	Parts List - Sample Preparation & Analysis	72

Chapter 1

Introduction

Scattering materials are ubiquitous, and they play key roles in fields such as tissue and blood analysis in medical imaging used to classify tumors as malignant or benign, produce characterization in the agriculture industry, soil analysis and material identification in remote sensing, and particle size estimates for quality assurance and shelf life estimates of cosmetics. These applications have widespread societal impacts, and they benefit from a deeper understanding of the optical properties of scattering. However, the complex nature scattering poses challenges for advancements in end applications. As a result, there has been a variety of approaches to understanding the underlying scattering phenomena. One class of approaches focuses on optically thick materials whose analysis can be approximated using the diffusion approximation. Monte-Carlo rendering has been used to consider materials of arbitrary thickness. However, they are computationally expensive and require proper initialization. The final class works under the single-scattering approximation and focuses on materials where single-scattering can be isolated. One way to isolate single-scattering is to dilute materials so light scatters once on average. This allows simple characterization methods similar to reflectometry for a narrow class of materials. Single-scattering can also be isolated for multi-scattering materials by using coherent illumination to compute scattering statistics dominated by single-scattered light. However, these methods have been limited to small scattering angles. The goal of this thesis is to combine the advantages of both approaches under the single-scattering approximation. We compute correlations to isolate single-scattered light in multi-scattering materials, and we expand the range of scattering angles from 8° to greater than 100° using scatteometry to make direct and accurate measurements for a broad class of materials.

1.0.1 Thesis contributions

In this thesis, we introduce a novel scatterometry system for material acquisition over a broad range of scattering angles exceeding 100°. We are particularly interested in opaque materials that exhibit multi-scattering. This thesis establishes the design approach for scatterometry under the single-scattering approximation as well as the calibration and alignment processes. The high-level design and unique aspects are detailed in Section [1.0.2](#), the calibration and alignment processes are covered in Sections [1.0.3](#), and results are discussed in Section [1.0.4](#).

1.1 Material acquisition (related work)

Material acquisition is the task of recovering the intrinsic properties of materials based on their appearance. It is of great importance in many applications. For example, tumors can be detected and classified as malignant or non-malignant [6]; important blood properties such as red and white blood counts can also be analyzed [4, 11]; in materials science, material acquisition is used to validate the fidelity and shelf life of material samples [35]; and the chemical compositions of nanodispersions can be inferred for particle sizing applications [32]. Material acquisition methods can be grouped into three categories depending on the ratio of the mean free path (expected distance traveled by a photon in the medium) to the characteristic size of the scattering volume. We summarize these categories in turn, as well as several common phase function models.

Inverse radiative transport [2] is studied heavily in graphics as well as the physical and biomedical sciences. While inverse radiative transport methods for scattering media fall into three main categories, methods using the *diffusion* approximation focus on optically thick media where high-order scattering is dominant. While this approximation simplifies inference and is suitable for both homogeneous and heterogeneous materials [13, 26, 31], it introduces parameter ambiguities. Similarity relations are hierarchical parameter relationships that allow scattering parameters to be altered without significantly altering the medium’s spatial properties. These relations can be derived from transport equations to accelerate Monte Carlo simulations [38]. However, a radiance field computed via Monte Carlo simulations can be described by multiple, distinct sets of parameters, and finding mulutiple candidate solution sets is generally challenging. Parameter space warping and exploiting similarity relations have improved the efficiency of iterative solvers [40].

Rather than focusing purely on high-order scattering, another class of methods considers all paths of arbitrary lengths. Given a set of input images, they estimate material parameters whose combinations closely match the inputs when simulated using Monte-Carlo rendering [12, 30]. Differentiable rendering

determines the effects of changes in scattering parameters by estimating derivatives of images. Traditionally, these estimates have been approximate models that ignore complex light transport effects such as subsurface scattering and inter-reflections [24]. Differentiable Monte Carlo rendering overcomes these limitations by computing derivatives while accounting for all light transport effects [16, 18, 23, 28, 29]. Machine learning approaches offer lower computational complexity at the cost of reduced robustness and diminished physically accurate solutions. Encoder networks can be paired with Monte Carlo renderers to improve their generalization to scenes with unseen geometry and light sources [37, 9]. Energy losses in neural radiance fields are mitigated by efficient indirect illumination estimation via spherical harmonics [41]. While these approaches are more general in nature and can handle arbitrarily thick materials, they are computationally expensive and require proper initialization.

The final class of methods are based on the *single scattering* approximation. The first approach assumes the medium is thin enough optically such that photons only scatter once when traveling through the medium. Since the scattering phase function is defined in terms of single-scattering, this allows the phase function to be observed directly. Although this method is as simple, it is limited to a narrow classes of materials such as gases and liquids of low viscosity [27]. Viscous liquids and thin solids can be acquired by illuminating materials with coherent light and computing the correlations of speckle images. Speckle image correlations are dominated by single-scattered light, and [1] showed that the phase function is proportional to the square root of the correlation and can be computed using a closed-form equation. However, this method is limited to measuring phase functions up to 8° due to aberrations.

The Henyey-Greenstein model is used widely due to its relative flexibility considering it is a single-parameter model [20]. It is controlled by an anisotropy parameter $g \in [-1, 1]$ that can be used to model backward and forward scattering. However, its simplicity limits its ability to accurately model other scattering regimes such as Rayleigh scattering that occurs when scattering particles are small compared to the wavelength [10, 33]. Alternatives to this model include using linear combinations of two Henyey-Greenstein lobes (forward and backward) as well as a two-parameter model for highly anisotropic scattering present in human blood [34]. However, there remain common materials that are not well-represented by these models such as soaps and waxes [17]. Hara et al. modify the HG phase function by adding side-lobes resembling the von Mises-Fisher distribution which closely resembles scattering of materials such as soaps and waxes that exhibit forward scattering with significant side scattering [14, 19].

1.2 Background

Scattering refers to the behavior of light when it interacts with a medium containing particles or when light interacts with the interface between two mediums of different properties. When light interacts with a particle in a scattering medium, the scattering event generates many additional light paths that all undergo additional scattering events before arriving at the observer. Scattering is essential to the appearance of food, liquids, skin, and other translucent materials, and an understanding of scattering is critical to determining their appearances. Under incoherent illumination, scattering produces smooth highlights with gradual falloff from the area of illumination. However, under coherent illumination, scattering produces speckle. Although speckle may appear random, it has a strong structure determined by the properties of the illumination and the scattering medium.

- Here's why we can reduce that to SS
- Once we have SS, this is how we make measurements

1.2.1 Scattering material representation

Scattering materials are generally composed of small particles with varying refractive properties we describe through the bulk statistical properties of the material. We use three statistical properties to parameterize the scattering material. The extinction coefficient describes the extinction cross-section of the scattering particles per unit volume. It is therefore proportional to the density of scattering particles inside the material. The extinction coefficient is the sum of the absorption and scattering coefficients $\sigma_t = \sigma_a + \sigma_s$ which represent, respectively, the portion of light absorbed and scattered per unit length along the path. The material's phase function $\rho(\arccos(\hat{\mathbf{i}} \cdot \hat{\mathbf{v}}))$ describes the directionality of scattered light and determines the portion of light scattered towards direction $\hat{\mathbf{v}}$ when a scatterer is illuminated from direction $\hat{\mathbf{i}}$. A scatterer's phase function is dictated by its shape and refractive index. Phase functions for spherical particles can be computed analytically using Mie theory[7, 15, 22]. ρ is generally assumed to be isotropic. This means its value depends only on the inner product of the illumination and viewing directions, and not on the absolute directions. This may be relaxed by adding an anisotropy parameter $-1 \leq g \leq 1$ where $g = -1$ corresponds to fully backward scattering, $g = 0$ means light is scattered equally in all directions, and $g = 1$ is full forward scattering. The mean free path (MFP) of a material is defined as the average distance light travels inside the volume between two successive scattering events. The MFP is the inverse of the extinction coefficient $MFP = 1/\sigma_t$. When working with scattering volumes, it is common to express its geometric dimensions with respect to the MFP. For example, a volume with

optical depth $OD = 4$ means its thickness is $4 \cdot MFP$. This means that light traveling through the medium is scattered four times on average.

Our work is primarily interested in the phase function ρ and will not discuss scattering coefficients. Our work seeks to acquire ρ as a general function and does not assume common parameterizations such as the Henyey-Greenstein phase function [20].

$$\rho_{HG}(\theta) = \frac{1}{4\pi} \frac{1 - g^2}{(1 + g^2 - 2g \cos \theta)^{3/2}} \quad (1.1)$$

1.2.2 Phase function from speckle images

Validating extended range phase functions Phase functions can be validated by comparing correlations to results computed from full Monte-Carlo simulations. Monodispersions of microscopic silica beads are well-suited for validation because their scattering effects are well described by Mie theory. Alterman et al. validate their results by comparing closed-form correlations from Equation ___ to results to a Monte-Carlo simulator [3] that has been verified against an accurate wave solver [36]. We assess our results in two. First, we verify our acquisition setup and single-scattering computations by comparing acquired $3\mu m$ and $10\mu m$ monodispersions to Mie theory. We then validate results for non-monodisperse samples that are not easily characterized for simulation (e.g., mustard, milk, honey) by comparing our acquired phase functions to those acquired by Alterman et al. over angular ranges up to approximately 8 degrees [1]. Given extended-range verification against theory and limited-range validation with related work, we consider our extended-range measurements valid.

Phase function from single scattering models A simple method for measuring phase functions is acquiring optically thin samples that scatter light once on average ($OD \approx 1$). This method is as simple as reflectometry: we illuminate a sample in direction i and measure the light received in direction v , and the phase function is the portion of energy corresponding to scattering angle $\arccos(\hat{i} \cdot \hat{v})$. In the paraxial regime, we can apply the small-angle approximation to equate the scattering angle as the norm of the displacement vector between the illuminating and viewing directions $\tau = \hat{v} - \hat{i}$, and $|\tau| = \arccos(\hat{i} \cdot \hat{v})$. This method fails with increasing material thickness due to multiple scattering.

1.3 Thesis contributions

Chapter 2

Speckle Correlation

Chapter 3

Scatterometer Design

In this chapter, we delve into the scatterometer design. We discuss the three main components of the scatterometer and their functions. We also detail unique design challenges for each component and any associated custom parts/accommodations that were necessary.

3.1 System design

Our scatterometer (detailed in Figures ?? and 3.2) consists of two mutually coherent, collimated beams of wavelength 532 nm separated vertically by a small angle of approximately 4° (assumed to be within the memory effect range for materials of interest). Both beams are attached to a stage that rotates the beams azimuthally about a scattering sample located on the stage's rotation axis. The intensity of scattered light is measured by a stationary camera as the beams are swept through a range of approximately 180°. The correlation of both beams' speckle images at a given azimuthal angle is proportional to the scattering phase function as a function of angle.

There are three primary components for acquisition. The first is the acquisition camera which we use to record speckle images. The second is the illuminator assembly which adjusts the angular illuminator separation and the azimuthal illumination direction relative to the acquisition camera. The third is the sample assembly which orients and positions the sample such that it is located on the azimuthal rotation axis of the illuminator assembly and maximal light is scattered towards the acquisition camera.

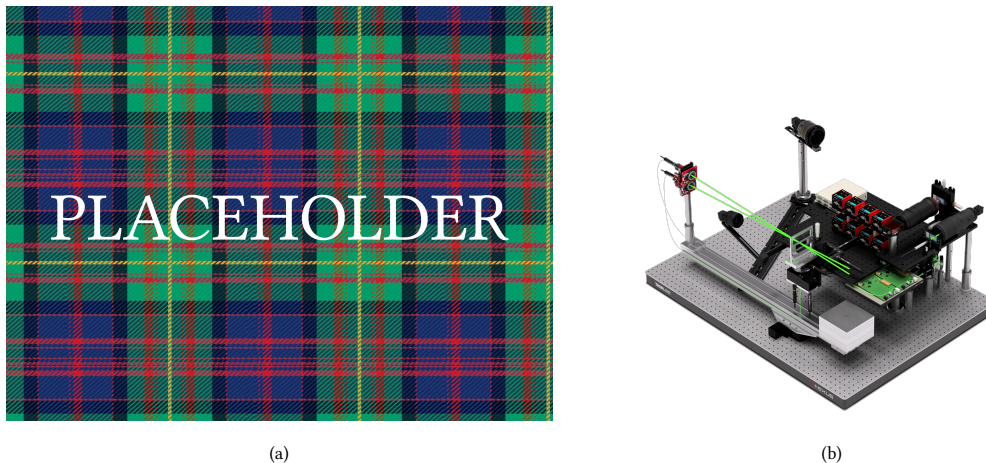


Figure 3.1: (a) Laboratory scatterometer setup; (b) CAD rendering of speckle correlation scatterometer

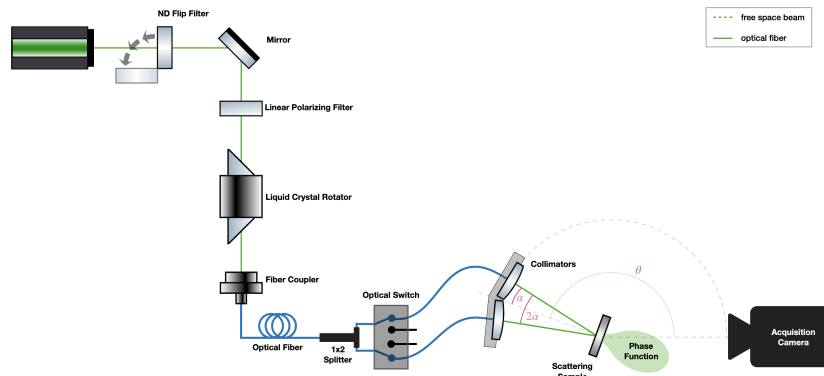


Figure 3.2: Light path diagram for speckle correlation scatterometer

Table 3.1: Illumination Configurations

Routine	Laser Power (mW)	ND Filter	Beam Diam. (mm)	Polarization Control
Kinematic calibration	160	0.0	1	No
Alignment	160	0.0	1	No
Camera calibration	160	6.3	1	No
Acquisition	20	3.0	5	Yes

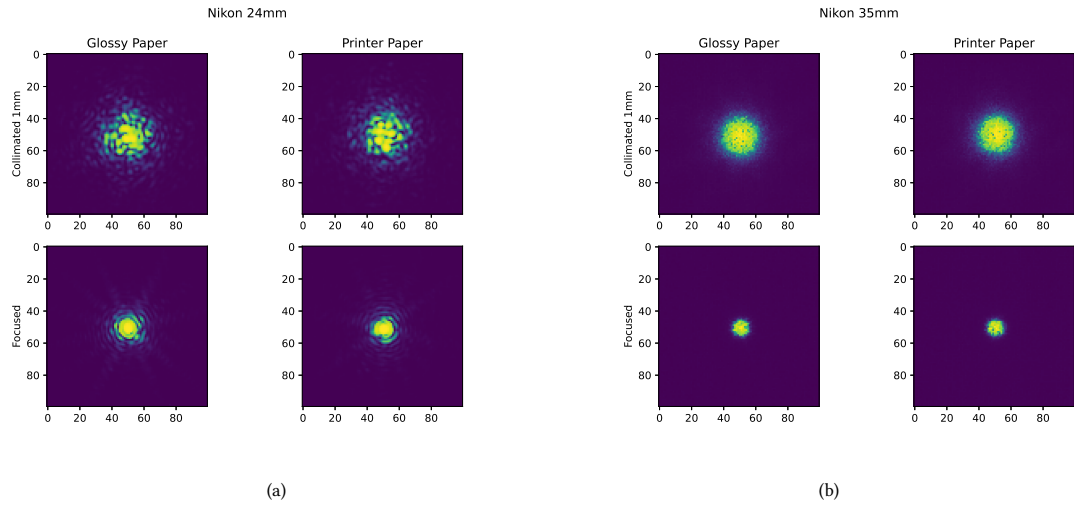


Figure 3.3: (a); (b)

3.1.1 Illumination

3.1.2 Reference Camera

3.1.3 Acquisition camera

The acquisition camera must record high-contrast speckle images and assign directions to light arriving at the camera. A desirable camera and lens combination is one that maximizes angular resolution and light efficiency. Therefore, we choose a camera with a large sensor and small pixel pitch, and a fast lens focused at infinity with a long focal length.

Lens Focal Length Computing the speckle correlation from images produced by the two illuminators requires both beams to fall within the camera’s FOV. Since we maximize single-scattered light by minimizing the illuminator separation, a lens with a small FOV corresponds to illuminators with a small angular separation. However, due to the finite size of the kinematic mounts, there is a minimum vertical separation. This minimum vertical separation and the FOV-limited angle between the beams define a triangle whose length is the distance from the illuminators’ kinematic mounts to the scattering sample. An 85 mm lens allows a small beam angle 2.47° relative to horizontal and an overall setup size that complies with space constraints.

We use a FLIR Grasshopper scientific camera model GS3-PGE-91S6M-C with an AF-S Nikkor 85 mm f/1.4G lens for acquisition.

Table 3.2: Acquisition camera specifications

Property	Spec
Camera Model	GS3-PGE-91S6M-C
Resolution	3376 × 2704
Megapixels	9.1
Pitch	3.69 μm
Sensor	Sony ICX814
Sensor Type	CCD
Sensor Size	12 × 10 mm
Spectrum	Mono
Lens Make	Nikkor
Lens Focal Length	85 mm
Lens Aperture	f/1.4
Lens Working Distance	∞

Lens Focal Length Computing the speckle correlation from images produced by the two illuminators requires both beams to fall within the camera’s FOV. Since we maximize single-scattered light by minimizing the illuminator separation, a lens with a small FOV corresponds to illuminators with a small angular separation. However, due to the finite size of the kinematic mounts, there is a minimum vertical separation. This minimum vertical separation and the FOV-limited angle between the beams define a triangle whose length is the distance from the illuminators’ kinematic mounts to the scattering sample. An 85 mm lens allows a small beam angle 2.47° relative to horizontal and an overall setup size that complies with space constraints.

3.1.4 Acquisition camera modifications

The acquisition camera’s CCD is protected from debris by a glass window. It is common practice to remove this window under coherent illumination since interference fringes are created when a portion



Figure 3.4

of light passing through the window is reflected internally. However, refraction caused by this window increases the effective focal length of the lens. Camera manufacturers account for this by offsetting the sensor's position along the optical axis so standard lens mounts can be used. Removing the window moves the focus closer to the front of the lens which is an issue when focusing at infinity since the focus will be always located in front of the sensor. The Fotodiox Nik-C (F to C) lens mount consists of a cylindrical component that interlocks with the F lens, and a conical component that matches the camera's C mount threads. To focus at infinity, we shortened the Fotodiox mount by machining 0.5 mm from its conical component to account for removing the glass window. The two lens mount components are secured using four radial screws which must be tightened evenly so their axes are aligned. We designed and 3D printed an alignment fixture that enforces their axial alignment during assembly. See Figure 3.4

3.1.5 Camera mount

During acquisition, we must place the camera in close proximity to the sample to maximize the solid angle over which we can acquire speckle. However, its position is in the path of the illuminator stand when it travels over a range of 230° during calibration. Therefore, we place the acquisition camera mount



Figure 3.5: (a); (b);

on an optical rail that allows us to slide it in and out of position. The base of the camera mount consists of a 1.5" post mounted to a rotation stage that slides along the rail and allows us to adjust the camera's orientation. We originally tried attaching the camera to the post using a lens collar, but we determined that the camera was unstable. Instead, we mounted the camera using threads on the inner front edge of the lens body and below the camera body. These two attachment points are mounted to a second rail that allows us to adjust the camera's position relative to the base to ensure both beams pass through the camera's aperture.

3.1.6 Illuminator Motion assembly

The illuminator motion assembly controls the illumination beams' directions both in azimuth and elevation. The primary design considerations are high angular resolution and repeatability for fine control of the illumination configuration, and structural stability to minimize vibrations. Each illuminator is attached to a 2-axis kinematic mount that allows $\pm 5^\circ$ in tip and $\pm 3^\circ$ in tilt. Both kinematic mounts are attached to a custom collimator mount that orients them as close as possible while complying with the FOV constraint of 4.93° between the illuminators. The collimator mount is attached to the azimuthal rotation stage via a rail whose length is 1 m. A desirable rail is 1) modular, offering flexibility in design and assembly, and 2) resistant to vibrations, thereby minimizing speckle blur during acquisition. Aluminum extrusions have T-slots and/or attachment points on multiple faces which help with ease of application. However, this advantage requires cross-sections that reduce the rail's resistance to deflection, and we seek to choose a rail that balances convenience with physical properties required for stable speckle acquisition.

Two relevant types of deflections studied in structural mechanics are beam bending and beam torsion. Beam bending refers to deflection caused by transverse forces/loads (e.g., a person standing on the end of a diving board), while torsion refers to angular deflection under torques (e.g., wringing a towel). First we will discuss relevant theory for beam bending and torsion. Then we will use the theory to establish our primary selection criteria. For the remainder of this section, "beam" will refer to a mechanical beam/rail unless otherwise specified.

Beam bending

Beam bending occurs when a force acts on a beam along a direction perpendicular to a chosen axis. In our case, we will discuss cantilever beams which are fixed at one end (allowing 0 degrees of freedom at its origin) and free at the other. A component with mass m under gravitational acceleration g creates a downward force with magnitude $F = mg$. When this force acts at a point located at ℓ along the beam, it creates a bending *moment of force*, or simply a *bending moment*

$$\mathbf{M} = \mathbf{F} \times \mathbf{\ell} \quad (3.1)$$

that causes the beam to bend downwards with deflection increasing from zero at its fixed end to its maximum distance at the location of the point load. We can use the maximum deflection equation to calculate the maximum beam deflection if the force, or load, acts at the free tip of a beam with length L

$$\delta = \frac{FL^3}{3EI_x}. \quad (3.2)$$

Under the assumption that the cross-section is in the x-y plane, we define I_x as the planar area moment of inertia which describes the beam's resistance to deflection in terms of the cross-section's mass distribution on both sides of the x-axis. We use the beam's x-axis since we are concerned with vertical loads caused by gravity that act along the y-axis. Under these assumptions, the planar area moment of inertia is a double integral over the cross-section area A

$$I_x = \iint_A y^2 dx dy. \quad (3.3)$$

E is the elastic modulus

$$E = \frac{\sigma}{\epsilon} \quad (3.4)$$

which describes the material's resistance to elastic (reversible) deflection. It is commonly written in units of GPa and expresses the amount of internal stress σ the beam experiences for a given change in its length ϵ where

$$\sigma = \frac{F}{A}, \quad \epsilon = \frac{\Delta L}{L} \quad (3.5)$$

Our primary interest is characterizing the beam's static resistance to bending (maximum deflection amplitude). The beam will also have a dynamic response that induces oscillations, but our illuminator motion assembly does not move in the vertical direction. We will assess the impact of ambient vibrations by inspecting speckle images for speckle blur.

Beam torsion

Extrusions commonly suffer from low torsional stiffness, meaning they have low resistance to twisting deformation. Twisting is generated when the azimuthal stage undergoes acceleration/deceleration. As the stage rotates at a rate of $\dot{\theta}$ rad s⁻¹, components mounted at a distance r from the rotation axis have a tangential velocity magnitude equal to $\|v\| = \dot{\theta}r$. When the stage comes to a rest, these components have inertia that requires a finite duration to come to rest after the stage has stopped moving, therefore causing them to lag behind the rail. During this lag, those components are undergoing deceleration, and they generate a force F that can be calculated using Newton's second law

$$F = m \frac{\Delta v}{\Delta t} \quad (3.6)$$

for a component with mass m and time variable t . This force is located at the component's center of mass, and it is perpendicular to the stage's rotation axis. If the neutral axis of the beam is located at a vertical position d relative to the component's center of mass, the force due to deceleration creates a twisting moment that causes the beam to twist (deform) about its neutral axis. We will refer to twisting forces that cause the beam to bend *along* its neutral axis as "moments", and we'll use "torques" to refer to twisting forces that cause angular beam deflection *about* its neutral axis. Assuming the deformation is elastic, the beam will have a restoring force that causes it to behave as a damped oscillator. These oscillations are ultimately transmitted to the illumination assembly and could cause speckle blur during acquisition. Our primary interest is characterizing the beam's static resistance to torsion, while we are also interested in calculating the damping ratio to determine a sufficient wait time for oscillations to decay between stage motion and data acquisition.

Torsional stiffness is a measure of a beam's resistance to deformation by torque. It is defined as the magnitude of torque T [N m] required to deflect a beam with length L by 1 radian

$$\frac{T}{\theta} = \frac{GJ}{L} \quad (3.7)$$

where J describes a beam's resistance to torsional deflection based on its geometrical properties. For circular and annular cross-sections, it is the polar moment of inertia

$$J_o = \iint_A r^2 dA \quad (3.8)$$

which is an area integral over the beam's cross section for infinitesimal area element dA located a distance r from the centroidal axis. For non-circular sections, it is called the torsional constant, which we will discuss below. G [Pa] is the shear modulus which is a measure of a material's stiffness independent of beam geometry

$$G = \frac{\tau_{xy}}{\gamma_{xy}} = \frac{F/A}{\Delta x/L} = \frac{FL}{A\Delta x} \quad (3.9)$$

where the shear stress $\tau_{xy} = F/A$ is the stress component that is coplanar with a cross section which has units of force per unit area (pressure), and $\gamma_{xy} = \Delta x/L$ is the cross-section's transverse displacement perpendicular to the cross-section plane's normal vector. Equation 3.8 only holds for circular cross-sections whose cross-sections undergo linear deformations. However, the theory is still useful when analyzing extrusion profiles which tend to be rectangular. For example, since the polar moment of inertia increases with the square of the distance of a differential area element from the centroidal axis, large cross-sections provide high resistance to torsion, which is further improved when solid regions of the cross-section are located near the edge of the beam profile. Modular extrusions generally have cross-sections that are empty near the center for weight reduction, which is not an issue. The slots that make them modular are located at the boundaries of their cross-sections, so we can conclude they generally have a low torsional moment of inertia, and consequently low torsional stiffness.

Profiles are generally characterized by their shear stress along *closed boundaries* inside their area profile. The total shear stress along a boundary s is defined

$$\oint_s \tau_{xy} ds = 2AGk \quad (3.10)$$

where k is the twist rate $d\theta/dz$ along the beam's length. Note that A is the *solid* area ($A_{solid} - A_{empty}$).

By rearranging Equation 3.10 to solve for the twist rate (angular beam deflection)

$$k = \frac{2AG}{\oint_s \tau_{xy} ds}, \quad (3.11)$$

we see that minimizing the twist rate (maximizing the torsional stiffness) is achieved by maximizing the length of the longest closed boundary in the cross-section assuming a given shear modulus and cross-sectional area. To consider the effect of wall thickness, we can use Bredt's formula to relate the shear stress induced by an external torque T for a beam with cross-section wall thickness t

$$\tau = \frac{T}{2At}, \quad (3.12)$$

and we can substitute this equation into Equation 3.10 to write a general expression for the polar moment of inertia of any thin-walled cross-section

$$J_o = \frac{4A^2}{\oint_s \frac{ds}{t}}. \quad (3.13)$$

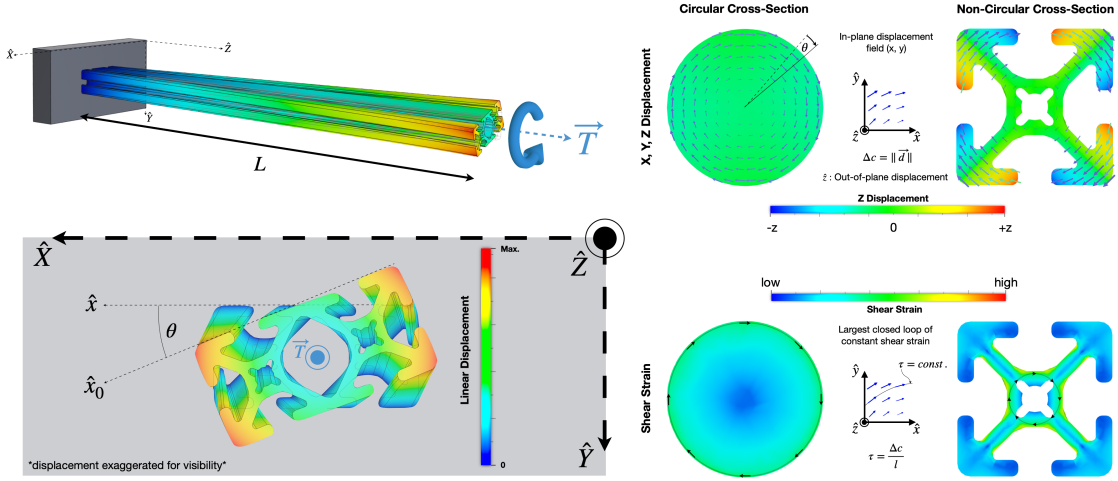


Figure 3.6: TODO: Replace with updated figure, add subfigure labels;

Now we can use the well-known total angular deflection equation to express the total deflection angle θ over the full length of the beam in terms of the polar moment of inertia

$$\theta = \frac{TL}{J_o G} = \frac{TLS}{4tA^2G} \quad (3.14)$$

where S is the length of the closed path enclosing the area A .

Torsional deformation of non-circular sections Recall that the polar moment of inertia J_o is computed in a plane. Circular cross-sections remain planar under torsion. However, non-circular section warps are not confined to a plane, and radial lines do not remain straight. In this case, we describe geometric resistance to torsion in terms of the *torsional constant* J which is bounded above by the polar moment of inertia ($J < J_o$). This is particularly relevant because aluminum extrusions are generally complex. Their cross-sections include multiple empty areas for weight reduction and modularity, as well as fins that increase the torsional constant and serve as slot reinforcements. In practice, the torsional constant is computed numerically, but there are formulas and approximations for common cross-sections used in structural mechanics [39]. The torsional constant for solid rectangular sections of size $a \times b$ is

$$J = \frac{ab^3}{16} \left[\frac{16}{3} - 3.36 \frac{a}{b} \left(1 - \frac{b^4}{12a^4} \right) \right]; \quad a \geq b. \quad (3.15)$$

3.1.7 Natural Bending Frequency

In progress [5].

$$f_1 = \frac{\lambda_1^2}{2\pi L^2} \sqrt{\frac{EJ}{\rho_L}} \quad (3.16)$$

Selection criteria From beam bending theory equation 3.2, the maximum bending magnitude is proportional to the cube of the beam’s length. However, its length is driven by our imaging configuration. The elastic modulus is fixed as well since we are only considering aluminum extrusions. Therefore, we minimize beam bending by choosing an extrusion with 1) a large cross-sectional mass distribution along its y-axis (large planar area moment of inertia). Additionally, equations 3.14 and 3.13, and 3.15 show that we minimize torsion by choosing cross-sections with 2) a large characteristic size, 3) high aspect ratio, and thick walls. Furthermore, 4) cross-sections that contain loops with maximal enclosed solid area are preferable, as well as 5) alloys with a high shear modulus. All selection criteria subject to space constraints and the azimuth stage’s maximum load rating.

Analysis

We analyze the structural properties of six aluminum extrusions whose cross-sections are summarized in Table 3.3. The cross-sections generally differ in overall size, aspect ratio, and wall thicknesses, with minor differences in material properties depending on the aluminum alloy. Our imaging configuration defines the illuminator assembly’s position and weight which create a moment M_i that will cause an imbalance. We choose the counterweight’s weight and position such that a counter-acting moment M_c that is equal and opposite of M_i such that $M_c = M_i$. If the illuminator assembly has mass m_i located at a distance r_i from the rotation axis, we can compute the counterweight’s mass m_c as a function of its location r_c along the rail

$$M_c = M_i \quad (3.17)$$

$$m_c r_c = m_i r_i \quad (3.18)$$

$$m_c r_c = 2.4 \cdot 0.686 \quad (3.19)$$

$$m_c = \frac{1.6}{r_c}. \quad (3.20)$$

We choose to minimize the overall weight of the assembly by placing the counterweight at the opposite end of the rail, which is 0.258 m from the azimuth rotation axis, meaning $m_c = 6.5$ kg. Table 3.4 shows the corresponding physical parameters used in our analysis. We focus solely on the illuminator for both the beam bending and torsion cases. It produces the largest bending deflection since its moment arm is approximately 2.7 times longer than the counterweight’s, and $\delta \propto L^3$. For torsion, both assemblies generate the same deceleration force, but the illuminator’s torque arm and moment arm are larger than the counterweight’s. Since $\theta \propto FdL$, the illuminator assembly produces larger deflection angles.

Table 3.3: Cross-sectional & material properties of aluminum extrusions [21]

Extrusion	XE25L-	1010	1020	1515	1530	1545
Vendor	Thorlabs	80/20	80/20	80/20	80/20	80/20
Width × Height (in.)	0.98 × 0.98	1.00 × 1.00	1.00 × 2.00	1.50 × 1.50	1.50 × 3.00	1.50 × 4.50
Solid Area (mm²)	281.51	279.67	744.16	507.65	1343.92	1928.42
Wall Thickness (mm)	2.02	2.21	2.21	4.06	4.06	4.06
Area Moment (cm⁴)	1.48	1.84	3.47	10.58	20.08	29.54
Aluminum Alloy	6000	6063-T6	6063-T6	6063-T6	6063-T6	6063-T6
Elastic Modulus (GPa)	68.95	68.95	68.95	68.95	68.95	68.95
Shear Modulus (GPa)	30.00	25.78	25.78	25.78	25.78	25.78

Table 3.4: Physical parameters for structural analysis assuming 12 deg/s azimuthal stage angular rate with 300 ms deceleration duration.

Assembly	Illuminator	Counterweight
Mass (kg)	2.4	6.5
Weight (N)	24.0	63.8
Distance Along Rail (m)	0.686	0.258
Bending Moment (N m)	16.5	16.5
Deceleration Force (N)	1.2	1.2
Torsion Arm (m)	0.231	0.083
Torsion Torque (N m)	0.3	0.1

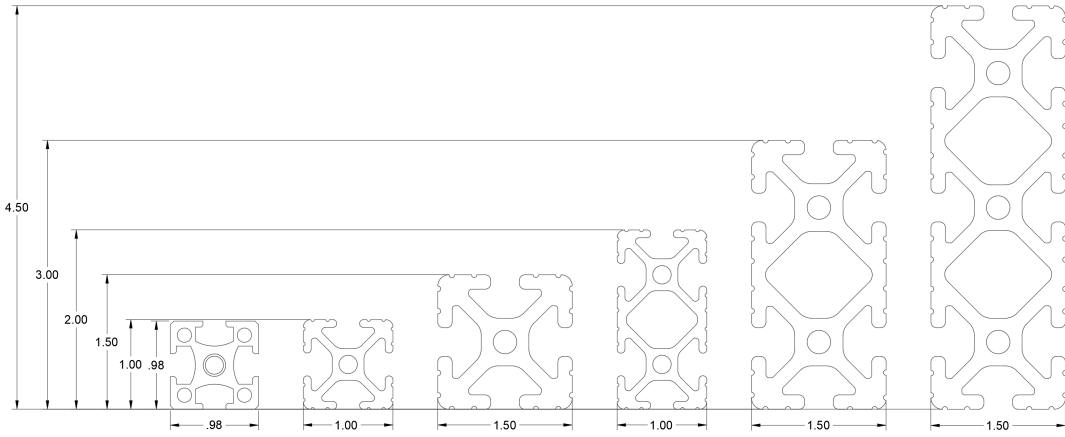


Figure 3.7: Aluminum extrusion profiles in order of increasing aspect ratio. All dimensions are in inches. TODO: ADD REINSERT CROSS-SECTION LABELS.

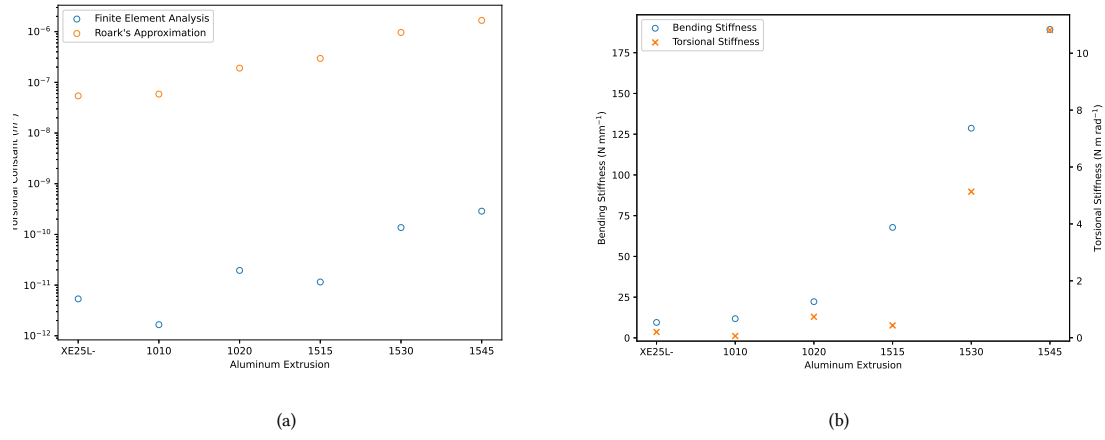


Figure 3.8: (a); (b)

Beam bending Figure ___ shows the beam bending free body diagram for our setup. The middle of the rail is fixed to the rotation by 14 bolts, so we assume either end of the rail does not affect the other, and we treat them independently. Since the area moment of inertia was published for each aluminum extrusion, maximum deflection for each extrusion was computed using Equation 3.2.

Beam torsion Equation 3.14 for maximum torsion deflection requires the torsional constant which must be computed numerically, so we compare candidate extrusions using finite element analysis (FEA). Although we simplify our analyses by assuming torques at each end are independent, it is not as strong

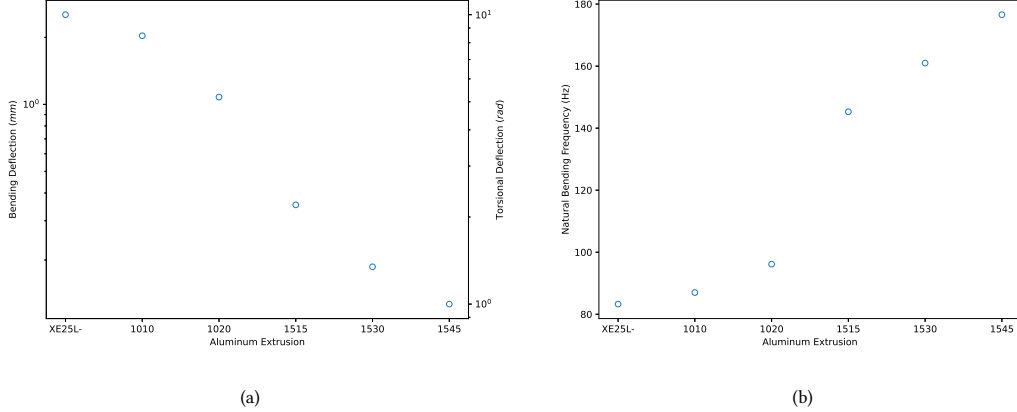


Figure 3.9: (a) Maximum beam bending and torsional deflection due to the illuminator assembly TODO: RERUN TORSIONAL ANALYSIS WITH UPDATED PARAMETERS; (b) Natural beam bending frequency due to the illuminator assembly

as the assumption we make for independent beam bending. Since torsion is caused by deceleration forces parallel to the plane of rotation, they will also generate oscillatory stage rotation that in turn affects beam torsion. Modeling this phenomena requires more complex analysis methods and is beyond the scope of our work.

In our simulations, we use a fixed support at one end of the beam, and we apply a torque at its free end that acts along the beam's long axis. We ran FEA simulations using Autodesk Fusion CAD software to compute the illuminator assembly's mass center of mass. We estimate the force component of the torque assuming the azimuthal stage is traveling 12 deg/s with an deceleration time of 300 ms. We computed the torsional stiffness of six different aluminum extrusions with cross-sections of varying sizes and aspect ratios. All six cross-sections are shown in Figure 3.7.

TODO: Use this paragraph to summarize why we chose to use 1530.

3.1.8 Collimator Mount

Calculates the design space for the collimator mount. Given acquisition camera position and FOV, it calculates valid combinations of 1) linear collimator separation 2) angular collimator separation $d_{camera} = 969.417$ mm $r_{aperture} = 26.73$ mm

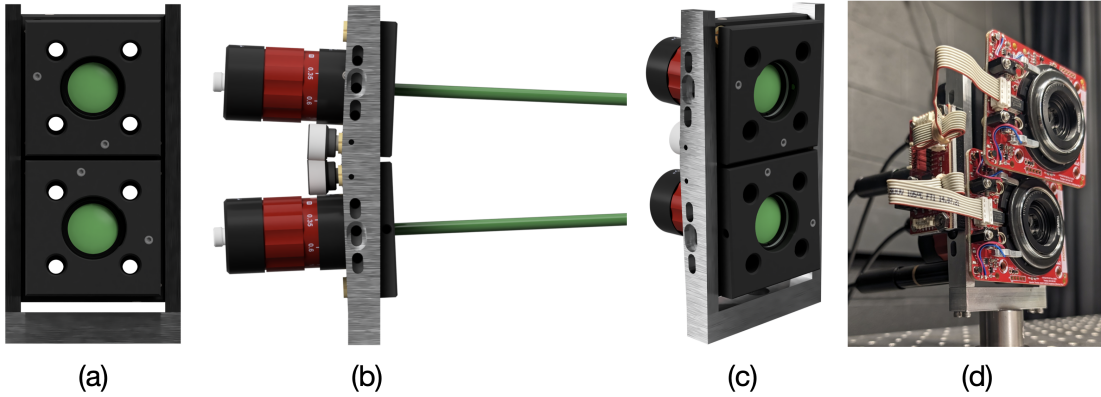


Figure 3.10: (a) CAD front view of collimator mount; (b) CAD side view showing the relative orientations of illumination beams; (c) CAD perspective view; (d) Fully assembled collimator mount which controls vertical and angular illuminator separation. Beam diameter is also controlled using motorized iris diaphragms.; TODO: Replace single collage with subfigures.

3.1.9 Sample assembly

The sample motion assembly's primary purpose during acquisition is to rotate the scattering sample so the amount of laser light scattered towards the camera is maximized since there are transmittive losses at air-glass interfaces as the illuminators' azimuthal position changes. This rotation is controlled by a small rotation stage which is mounted on an XYZ stage and an tip/tilt stage. These additional stages are used to control the rotation stage's orientation so it can made to be collinear with the illuminator assembly's azimuthal rotation axis. There is an additional translation stage mounted to the rotation stage's motion plate that is used to align the center of a mounted sample with the upper- and lower motion stages' rotation axes.

The sample mount is a custom, dual purpose mount used to hold scattering samples during acquisition and checkerboard targets during calibration. It is designed such that the front face of a calibration target is in the same plane as the central plane of a scattering sample. It consists of a base and angle mounts used to attach a square aluminum frame that holds a 10×10 cm glass window in place through compression by tightening four thumbscrews. Scattering samples are mounted by removing the aluminum frame's front face and attaching an inset frame that holds microscope slides via compression.

3.1.10 Illumination polarization control

The Verdi output beam is linearly polarized and passed through single-mode (SM) fibers prior to illuminating scattering samples with the resulting beam having an unknown polarization state due to use of non-polarization-maintaining fibers. This raises several questions 1) What is the beam's polarization

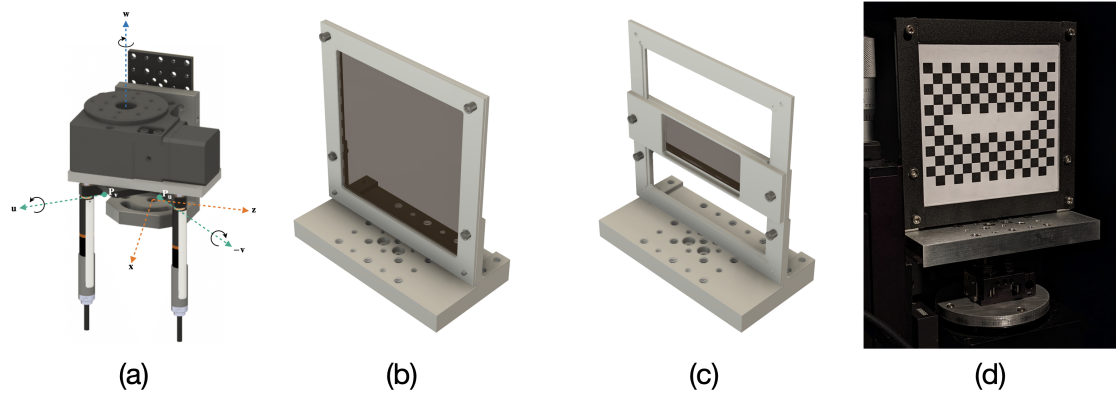


Figure 3.11: (a) Sample motion assembly without sample mount; (b) Sample mount configured for calibration target (not drawn to scale with respect to (a)); (c) Sample mount configured for scattering sample on a microscope slide (not drawn to scale with respect to (a)); (d) Sample mount shown on top of sample assembly with calibration target installed

state?; 2) Is it constant?; and 3) What is the optimal polarization state of the output beam to maximize light transmission into the sample?

Literature suggests the output beam will have an elliptical polarization state (1) that is variable/unstable (2) due to variable birefringence induced in SM fibers caused by variable internal stresses and temperature fluctuations.

The output polarization state's stability was characterized by placing a power meter photodiode with a static LPF to measure the power of a collimator on the dual collimator stand attached to the RT-5 rail. The measured power for 10 sweeps of the RT-5 through a range of 280 degrees is shown in Figure 3.12. There is a clear relationship between the measured power through an LPF and the RT-5 stage position which suggests the polarization state does not remain constant across illumination angles. The ellipticity was not investigated due to requiring a circular polarizing filter (CPF). Fluctuations in measured power across sweeps was due to insertion losses caused by motion of unstable FC/PC fiber connectors on the RT-5 rail. Fixing those connectors to the rail saw significant reductions in fluctuations.

Polarization state for Figure 3.12:

- $S_0 = 0.200696$
- $S_1 = -0.028441$
- $S_2 = 0.06834$
- $S_{DoP} = \sqrt{S_1^2 + S_2^2}/S_0 \approx 0.37$

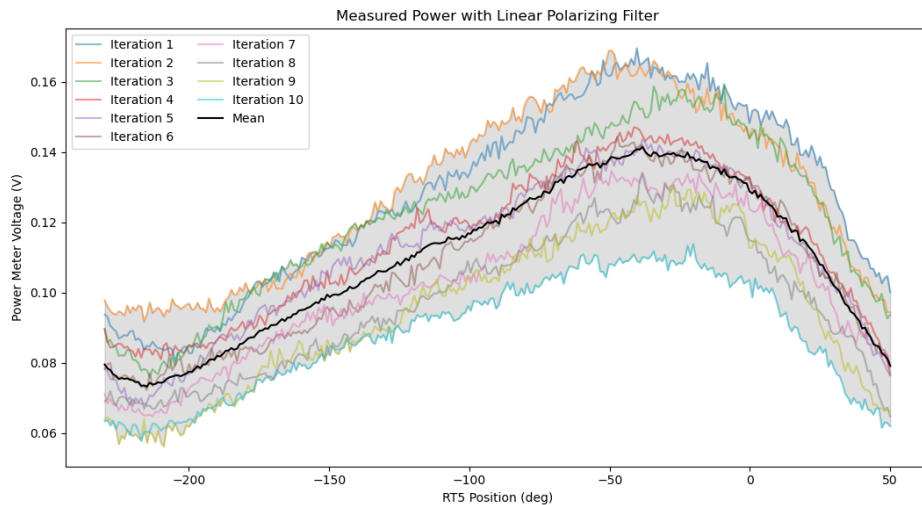


Figure 3.12

We tried depolarizing the free space input and output beams. For input depolarization, we still saw changes in the illumination polarization state as the RT-5 moved. For output depolarization, the beam's polarization state varied spatially meaning we'd illuminate different parts of the sample with different polarization states which would affect our correlations

Liquid crystal rotator

3.2 Sample Analysis Station

We characterize each scattering sample by measuring its optical density and its particle density along its thickness. We measure optical density by comparing the power of ballistic laser laser before and after it has passed through a scattering sample. The laser is the same wavelength as the acquisition laser, and images are acquired using a Point Grey GS3-PGE-91S6M-C scientific camera with an AF Micro-Nikkor 200mm f/4D focused at infinity. We measure particle density as a function of depth by computing particle area density for each image in a focal stack. The microscope imager is an Allied Vision Prosilica GT3400 scientific camera whose lens consists of a Canon 180mm f/3.5 L EF Macro lens and a 0.65NA 40X Olympus Plan Achromat Obective

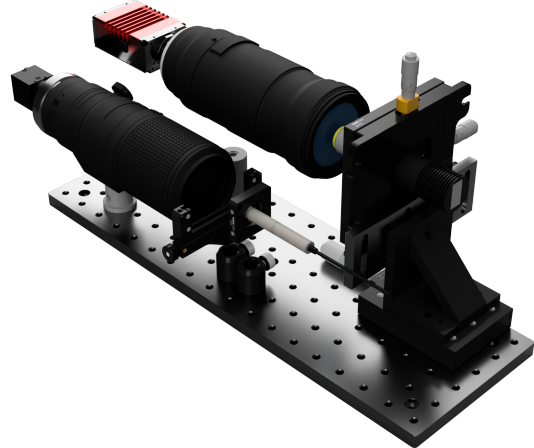


Figure 3.13: CAD rendering of the sample analysis station

Chapter 4

Scatterometer Calibration and Alignment

In this chapter, we detail the scatterometer calibration and alignment processes.

4.1 Calibration and alignment

1. Kinematic calibration
2. Sample motion assembly calibration
3. Sample motion assembly alignment
4. Illumination alignment
5. Beam estimate update
6. Target alignment
7. Acquisition camera calibration

4.2 Calibration Targets

We use two primary checkerboard calibration targets for beam direction and pose estimation during scatterometer calibration and alignment. The first is a 12×15 checkerboard with 6.1mm spacing mounted on both faces of a 10×10 cm Corning Gorilla Glass window. This target is used primarily for estimating rotation and translation stage axes and motion stage pose. The other primary target uses the same checkerboard size, but it is one-sided, and it is missing a 2×9 block of checkerboard squares at its center.

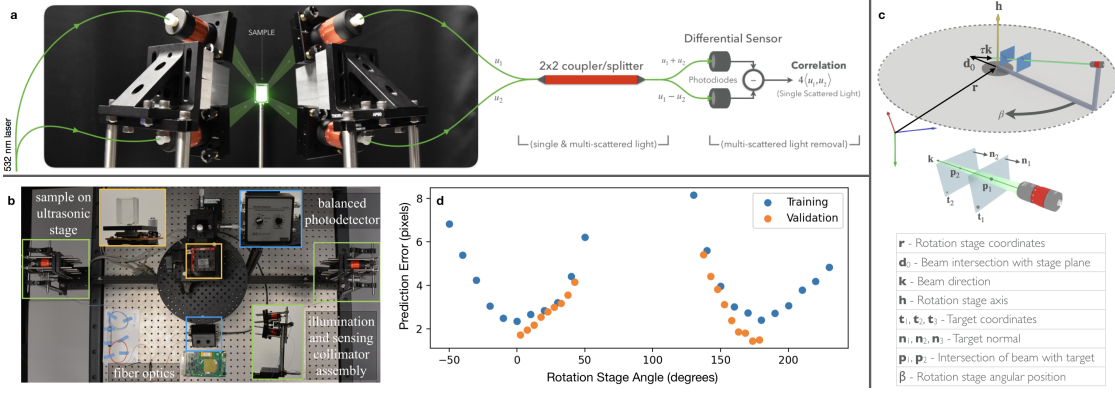


Figure 4.1: a: Speckle correlation computation pipeline. The sample is illuminated by two beams, and the correlation is computed using a differential sensor. b: Physical setup with sample placed on the circular breadboard. The illumination stand rotates about the sample while the sensing stand measures scattered light. The differential photodetector enables fast correlation computation. c: Geometry used to develop forward model for inverse problem estimation of 3D beam-plane intersection points. d: Mean estimation errors for training and validation phases showing angular dependence of error.

We explored many checkerboard sizes and found that squares sizes smaller than 5mm produced noisy MATLAB camera calibration. We chose 6.1mm squares since it maximizes the checkerboard density while producing stable MATLAB camera calibration. Both targets are laser printed on standard office printer paper, so their actual sizes will differ from their intended sizes due to printer scaling, paper texture, and limited printing precision. One issue with the relatively small square size is that these printing errors become larger with respect to the square size, and errors of approximately 1% can cause a depth error estimate of greater than 3mm. However, we were only able to measure their sizes to an accuracy of 3.5%. We use a third 18×25 (7.5mm square size) calibration target that is UV printed on a rigid, low-density polyethylene board (LDPE) with 0.04mm precision as a reference. We determine the laser printed targets' square sizes in the following manner. We place all three targets at the same depth, and we estimate the reference target's depth assuming its nominal dimensions as ground truth. For each laser printed target, we find the square size that minimizes the difference between its depth and the reference target's depth. We verified our results by laser printing all targets on the same sheet of paper and confirming all three square size estimates were similar down to tens of microns. We detail the effects of albedo and square size analyses in Appendix 7.1.

4.3 Lower Stage Calibration

The goal of calibrating the lower assembly is to estimate its rotation axis and the 3D orientation of the illumination beams as a function of the azimuth angle θ . We do so by computing the 3D intersection of

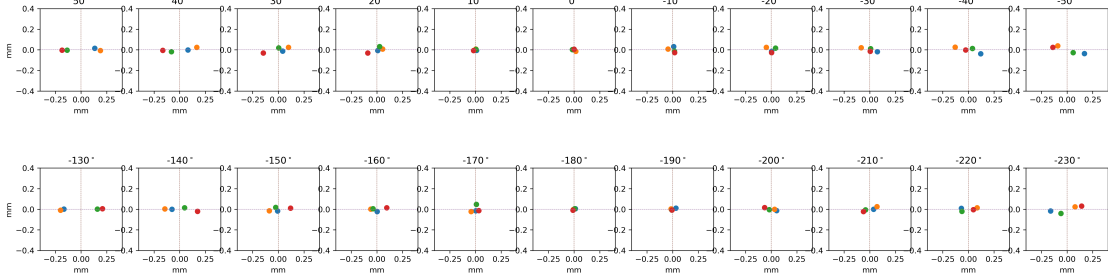


Figure 4.2: Perpendicular offsets of the four observed beam-plane intersections with respect to the estimated beam direction. Each plot is for an azimuthal angle $\theta \in \Theta$. The cause of increasing perpendicular offsets for increasing angle with respect to the plane normal and anti-normal is unknown.

each illumination beam with a series of N planes whose poses we know. This process is repeated for all $\theta \in \Theta$ for a total of $2N|\Theta|$ points. From this set of points, we can estimate the illumination directions for both beams as a function of θ and the azimuth stage pose up to a rotational ambiguity about its rotation axis.

Azimuth Stage Rotation Axis Each beam is associated with a set of $N|\Theta|$ points. Define a set of difference vectors $\{\tilde{k}_\theta\}$, $|\{\tilde{k}_\theta\}| = L$ as the differences between all N permute 2 points along a ray. We define a ray as a beam located at any particular $\theta \in \Theta$. Each \tilde{k}_θ makes an angle $\pi/2 - \alpha$ with the rotation axis. However, the $L P_2$ second order difference vectors are perpendicular to the azimuth rotation axis \hat{h} , and we estimate \hat{h} as their null space.

Beam Direction for $\theta = 0$ Once we know the azimuth rotation axis, we can use it to estimate both illuminators' beam directions. For each $\theta \in \Theta$, we compute the centroid $\bar{p}_\theta = \frac{1}{N} \sum p_n$. We subtract the centroid from the point set so it is zero mean and rotate it about \hat{h} by $-\theta$ so all points are aligned with $\theta = 0$. The beam direction k_0 is simply the point set's principal component.

4.3.1 Stage Position & Beam Direction as a Function of θ

Assume a collimated beam fixed to a rotation stage with location r and rotation axis \hat{h} . If the stage is rotated 360 degrees, the pencil of rays created by the rotated beam will form a paraboloid with axis \hat{h} and small radius ρ equal to the distance of closest encounter of the beam with the paraboloid axis. The locus of these points of closest encounter constitutes the beam's ray envelope. Note: Insert ray envelope theory The isoline of the ray envelope is

$$c(\theta) = r + \delta\hat{h} + r(\theta)\rho_0, \quad (4.1)$$

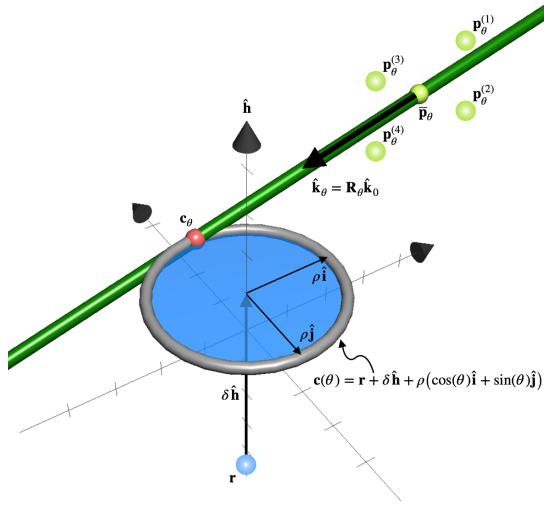


Figure 4.3: RT-5 Geometry - Frustrum top Surface

where δ is the height of the circle above the stage, ρ is a 2×1 vector. $r(\theta)$ is a 3×2 matrix consisting of a rotation of two basis vectors \hat{i} and \hat{j} through an angle of θ about the rotation axis \hat{h} with each basis vector being perpendicular to \hat{h}

$$r(\theta) = R(\hat{h}, \theta) \begin{bmatrix} \hat{i} & \hat{j} \end{bmatrix}, \quad R(\hat{h}, \theta) \in \mathbb{R}^{3 \times 3}. \quad (4.2)$$

If M points $p_\theta^{(1)}, p_\theta^{(2)}, \dots, p_\theta^{(M)}$ are measured along the ray at a given rotation stage position $\theta \in \Theta$, then the beam with direction \hat{k}_θ passes through their centroid \bar{p}_θ with its pencil defined

$$l_\theta(s) = \bar{p}_\theta + s\hat{k}_\theta \quad (4.3)$$

4.3.2 Azimuth Stage Location

Given the problem formulation, the objective is to find the circular conic section with perimeter $c(\theta)$ by choosing r such that the circle's radius ρ is minimized. We achieve this by computing the minimum distance of each beam from the axis of rotation and minimizing the variance across all angles:

$$\min_r g_2(r) \quad (4.4)$$

$$\min_r \sigma^2(\{\rho_\theta\}) \quad (4.5)$$

$$\min_r \sum_{\theta \in \Theta} (\rho_\theta - \bar{\rho})^2 \quad (4.6)$$

where

$$\rho_\theta = \hat{\mathbf{n}}_\theta^\top (\bar{\mathbf{p}}_\theta - \mathbf{r}), \quad \hat{\mathbf{n}}_\theta = \frac{\hat{\mathbf{k}}_\theta \times \hat{\mathbf{h}}}{\|\hat{\mathbf{k}}_\theta \times \hat{\mathbf{h}}\|}, \quad \bar{\rho} = \frac{1}{|\Theta|} \sum \rho_\theta \quad (4.7)$$

We minimize the objective by computing its partial derivative with respect to \mathbf{r} . Firstly, we define

$$\bar{\mathbf{n}}_{\bar{\mathbf{p}}} = \frac{1}{|\Theta|} \sum \hat{\mathbf{n}}_\theta^\top \bar{\mathbf{p}}_\theta, \quad \bar{\mathbf{n}} = \frac{1}{|\Theta|} \sum \hat{\mathbf{n}}_\theta, \quad (4.8)$$

and compute the partial derivative with respect to \mathbf{r} :

$$\frac{\partial g_2(\mathbf{r})}{\partial \mathbf{r}} = \sum_\theta (\rho_\theta - \bar{\rho})(\bar{\mathbf{n}} - \hat{\mathbf{n}}_\theta) \quad (4.9)$$

$$= \sum_\theta \left[-(\hat{\mathbf{n}}_\theta^\top \bar{\mathbf{p}}_\theta) \hat{\mathbf{n}}_\theta + (\hat{\mathbf{n}}_\theta^\top \mathbf{r}) \hat{\mathbf{n}}_\theta + \bar{\mathbf{n}}_{\bar{\mathbf{p}}} \hat{\mathbf{n}}_\theta - (\bar{\mathbf{n}}^\top \mathbf{r}) \hat{\mathbf{n}}_\theta + (\hat{\mathbf{n}}_\theta^\top \bar{\mathbf{p}}_\theta) \bar{\mathbf{n}} - (\hat{\mathbf{n}}_\theta^\top \mathbf{r}) \bar{\mathbf{n}} - \bar{\mathbf{n}}_{\bar{\mathbf{p}}} \bar{\mathbf{n}} + (\bar{\mathbf{n}}^\top \mathbf{r}) \bar{\mathbf{n}} \right] \quad (4.10)$$

$$= \sum_\theta \left[-(\hat{\mathbf{n}}_\theta^\top \bar{\mathbf{p}}_\theta) \hat{\mathbf{n}}_\theta + \bar{\mathbf{n}}_{\bar{\mathbf{p}}} \hat{\mathbf{n}}_\theta + (\hat{\mathbf{n}}_\theta^\top \bar{\mathbf{p}}_\theta) \bar{\mathbf{n}} - \bar{\mathbf{n}}_{\bar{\mathbf{p}}} \bar{\mathbf{n}} \right] + \sum_\theta \left[(\hat{\mathbf{n}}_\theta^\top \mathbf{r}) \hat{\mathbf{n}}_\theta - (\bar{\mathbf{n}}^\top \mathbf{r}) \hat{\mathbf{n}}_\theta - (\hat{\mathbf{n}}_\theta^\top \mathbf{r}) \bar{\mathbf{n}} + (\bar{\mathbf{n}}^\top \mathbf{r}) \bar{\mathbf{n}} \right] \quad (4.11)$$

We define

$$\mathbf{N}_\theta = \sum_\theta \hat{\mathbf{n}}_\theta \hat{\mathbf{n}}_\theta^\top, \quad \bar{\mathbf{N}}_\theta = \sum_\theta \hat{\mathbf{n}}_\theta \bar{\mathbf{n}}^\top, \quad \bar{\mathbf{N}} = \sum_\theta \bar{\mathbf{n}} \bar{\mathbf{n}}^\top, \quad (4.12)$$

set the partial derivative equal to zero, and rearrange it to the form $\mathbf{Ax} = \mathbf{b}$:

$$\sum_\theta \left[\hat{\mathbf{n}}_\theta \hat{\mathbf{n}}_\theta^\top - \hat{\mathbf{n}}_\theta \bar{\mathbf{n}}^\top - \bar{\mathbf{n}} \hat{\mathbf{n}}_\theta^\top + \bar{\mathbf{n}} \bar{\mathbf{n}}^\top \right] \mathbf{r} = \sum_\theta \left[(\hat{\mathbf{n}}_\theta^\top \bar{\mathbf{p}}_\theta) \hat{\mathbf{n}}_\theta - \bar{\mathbf{n}}_{\bar{\mathbf{p}}} \hat{\mathbf{n}}_\theta - (\hat{\mathbf{n}}_\theta^\top \bar{\mathbf{p}}_\theta) \bar{\mathbf{n}} + \bar{\mathbf{n}}_{\bar{\mathbf{p}}} \bar{\mathbf{n}} \right] \quad (4.13)$$

$$(\mathbf{N}_\theta - \bar{\mathbf{N}}_\theta - \bar{\mathbf{N}}_\theta^\top + \bar{\mathbf{N}}) \mathbf{r} = \sum_\theta (\hat{\mathbf{n}}_\theta^\top \bar{\mathbf{p}}_\theta) \hat{\mathbf{n}}_\theta - \bar{\mathbf{n}}_{\bar{\mathbf{p}}} \sum_\theta \hat{\mathbf{n}}_\theta + \left(- \sum_\theta \hat{\mathbf{n}}_\theta^\top \bar{\mathbf{p}}_\theta + \sum_\theta \bar{\mathbf{n}}_{\bar{\mathbf{p}}} \right) \bar{\mathbf{n}} \quad (4.14)$$

$$(\mathbf{N}_\theta - 2\bar{\mathbf{N}}_\theta + \bar{\mathbf{N}}) \mathbf{r} = \sum_\theta (\hat{\mathbf{n}}_\theta^\top \bar{\mathbf{p}}_\theta) \hat{\mathbf{n}}_\theta - \bar{\mathbf{n}}_{\bar{\mathbf{p}}} |\Theta| \bar{\mathbf{n}} + \left(- |\Theta| \bar{\mathbf{n}}_{\bar{\mathbf{p}}} + |\Theta| \bar{\mathbf{n}}_{\bar{\mathbf{p}}} \right) \bar{\mathbf{n}} \quad (4.15)$$

$$(\mathbf{N}_\theta - 2\bar{\mathbf{N}}_\theta + \bar{\mathbf{N}}) \mathbf{r} = \sum_\theta (\hat{\mathbf{n}}_\theta^\top \bar{\mathbf{p}}_\theta) \hat{\mathbf{n}}_\theta - |\Theta| \bar{\mathbf{n}}_{\bar{\mathbf{p}}} \bar{\mathbf{n}} \quad (4.16)$$

We solve equation 4.16 with the equality constraint $\hat{\mathbf{h}}^\top (\mathbf{r} - \mathbf{t}_2) = 0$. The resulting RT-5 location \mathbf{r} is similar to the estimate in the first method with a displacement vector norm of only 0.001 mm, and the mean distance $\bar{\rho} = 0.42$ mm (as expected).

4.3.3 Ray Envelope Center

Given \mathbf{r} and $\{\rho_\theta\}_\Theta$, a point \mathbf{c}_θ is defined on each ray such that its distance from the RT-5 axis is equal to ρ_θ .

$$\mathbf{c}_\theta = \bar{\mathbf{p}}_\theta + t_\theta \hat{\mathbf{k}}_\theta \quad (4.17)$$

where

$$t_\theta = \frac{\mathbf{m}_\theta^\top \mathbf{B}(\mathbf{r} - \bar{\mathbf{p}}_\theta)}{\mathbf{m}_\theta^\top \mathbf{B}\hat{\mathbf{k}}_\theta}, \quad \mathbf{m}_\theta = \hat{\mathbf{n}}_\theta \times \hat{\mathbf{k}}_\theta \quad (4.18)$$

Given the set $\{\mathbf{c}_\theta\}_\Theta$, we solve the following minimization problem to find the optimal center of the circular ray envelope $\mathbf{r} + \delta\hat{\mathbf{h}}$ whose radius is $\bar{\rho}_\theta$ and minimizes the sum of the squared distances of points from the circle:

$$\begin{aligned} & \min_{\delta} g_3(\mathbf{r}, \delta, \mathbf{c}_\theta) \\ & \min_{\delta} \sum_{\theta \in \Theta} (\|\mathbf{c}_\theta - \mathbf{r} - \delta\hat{\mathbf{h}}\|^2 - \bar{\rho}^2)^2. \end{aligned} \quad (4.19)$$

The partial derivative with respect to δ is

$$\frac{\partial g_3(\mathbf{r}, \delta, \mathbf{c}_\theta)}{\partial \delta} = 4|\Theta|\delta^3 + 3B\delta^2 + 2C\delta + D = 0 \quad (4.20)$$

where

$$B = 4\hat{\mathbf{h}}^\top \sum (\mathbf{r} - \mathbf{c}_\theta), \quad C = 2 \sum [2(\mathbf{r} - \mathbf{c}_\theta)^\top \hat{\mathbf{h}}\hat{\mathbf{h}}^\top (\mathbf{r} - \mathbf{c}_\theta) + \|\mathbf{c}_\theta\|^2 - 2\mathbf{c}_\theta^\top \mathbf{r} + \|\mathbf{r}\|^2], \quad (4.21)$$

$$D = 4\hat{\mathbf{h}}^\top \sum (\mathbf{r} - \mathbf{c}_\theta)(\|\mathbf{c}_\theta\|^2 - 2\mathbf{c}_\theta^\top \mathbf{r} + \|\mathbf{r}\|^2) \quad (4.22)$$

The partial derivative is a third degree polynomial whose roots minimize the objective function $g_3()$. We find its roots via the `roots()` method from the `numpy.polynomial.Polynomial` class.

4.3.4 Ray Envelope Isoline

We find its radius and orientation defined by the vector $\boldsymbol{\rho}_0$ such that $\mathbf{c}(0) = \mathbf{r} + \delta\hat{\mathbf{h}} + \boldsymbol{\rho}_0$ is the point on the ray envelope corresponding to azimuthal position 0° . Given \mathbf{r} and δ , and a set of points $\{\mathbf{c}_\theta\}$ defined by the intersections of rays with the ray envelope plane, we can solve for the least-squares optimal $\boldsymbol{\rho}_0$ using Equation 4.1:

$$\min_{\boldsymbol{\rho}_0} \sum_{\theta} \|R_\theta \boldsymbol{\rho}_0 - (\mathbf{c}_\theta - \mathbf{r} - \delta\hat{\mathbf{h}})\| \quad (4.23)$$

4.3.5 Training & Validation Datasets

The training set consists of 22 rotation stage positions in 10° increments spanning $\pm 50^\circ$ relative to the normal on both faces of a target, totaling 100° and a measurement for each target. The differences of these 3D point-plane intersections are computed as the initial beam direction estimates $\bar{\mathbf{k}}$. Given a learned model, the objective is to predict point-plane intersections for new planes and angles. The

similar to training but with random target positions and a smaller angular sweep. Actual phase function measurements will be constrained to a 180° range. Therefore, the validation set consists of angles within this range, each offset from training angles by 5° .

4.4 Sample Motion Assembly Calibration

The goal in calibrating the sample motion assembly is estimating the primary rotation stage's pose as well as the translation and rotation axes of all stages used to position and orient the rotation stage.

Rotation Stage Pose Estimating the rotation stage pose is similar to the method used to estimate the azimuthal rotation axis. Rather than rotating a laser and computing beam-plane intersections, we take photos of a series of N rotated planes and detect a 3D grid of M points on each plane. NP_2 1st-order difference vectors are computed for each of the M points in the grid totaling $M(NP_2)$ vectors that are in the plane of rotation. The rotation axis $\hat{\mathbf{w}}$ is perpendicular to the plane of rotation and is therefore the null space of the vector set.

Translation Stage Axes All translation stage axes are estimated by computing 3D coordinates of checkerboard corners at several positions along the translation stage's range of motion. Difference vectors are computed for all combinations of corresponding points on the planes, and the axis is the mean of all difference vectors. The vector is oriented to point in the direction of increasing stage position.

Tip & Tilt Stage Axes The sample assembly is oriented using a 2-axis tip/tilt kinematic stage. These axes are not used in any analytical expressions; they are simply used as a 2D basis for azimuthal rotation axis PID alignment. Their limited range of motion and image noise produce unstable estimates, so visually approximated estimates are sufficient as long as the axes are perpendicular.

4.5 Aligning Sample and Illuminator Assemblies

The sample and illuminator assemblies are aligned when their rotation axes are collinear.

4.5.1 Rotation

We define a plane Π with normal vector $\hat{\mathbf{h}}$ and origin $p_{\hat{\mathbf{h}}}$. This plane defines a basis with projection matrix $\Pi \in \mathbb{R}^{2 \times 3}$ whose rows are in the null space of $\hat{\mathbf{h}}$. The sample assembly's rotation axis $\hat{\mathbf{w}}$ is aligned with the azimuthal axis when its projection $\Pi\hat{\mathbf{w}} = \mathbf{0}$. For PID control we seek to express the alignment

error vector $\epsilon = \Pi\hat{w}$ in terms of two independent error components ϵ_u and ϵ_v controlled by u- and v-axis rotation respectively. Since rotation affects motion in a plane perpendicular to the axis, and the tip and tilt axes are perpendicular, we can express the alignment errors independently by defining a new error vector ϵ' in terms of a modified basis $\Pi' = \Pi[\hat{u} \ \hat{v}]$. The new error vector is

$$\epsilon' = \begin{bmatrix} \epsilon'_v \\ \epsilon'_u \end{bmatrix} = \Pi'\hat{w}. \quad (4.24)$$

Note the swapped order of the elements in the error vector due to perpendicularity: the u-axis error is the projection of \hat{w} onto the v-axis, and the v-axis error is the projection of \hat{w} onto the u-axis. This modified basis preserves the mapping of zero alignment error to the zero vector.

Although the tip and tilt axes are perpendicular, they are not independent since the square motion plate is actuated at opposite corners with a shared ball joint pivot point at another. Therefore, the alignment loop alternates between the u- and v-axis PID controllers with state error updates between each controller. The stage has limited range of motion due to space constraints, so we use the Zielger-Nichols "no overshoot" gain configuration.

Translation Once the two rotation axes are parallel, we use the x- and z-axis translation stages to make the collinear.

4.6 Aligning Calibration Target with Sample Motion Assembly Rotation Axis

The compact translation stage mounted on top of the RT-3 stage is used to position the calibration target locally such that the RT-3's rotation axis intersects the calibration target's surface at the height of a scattering sample. The stage is calibrated per Paragraph 4.4. The alignment error is computed by first defining a horizontal line on the calibration target positioned along the midline of the scattering sample. Define the minimum-length displacement vector between the two axes as δ . The error is then the projection of δ onto the stage's translation axis m .

Define the mean beam direction vector $\bar{k} = (\hat{k}_0^{(a)} + \hat{k}_0^{(b)})/2$. For target with plane normal \hat{z} , the objective is

$$\min_{\psi} 1 - \bar{k}^T \hat{z}(\psi) \quad (4.25)$$

where $\hat{z}(\psi) = R_{\hat{w}}\hat{z}_0$ is the initial normal vector rotated about \hat{w} by an angle ψ .

Two points P_1, P_2 on plane Π_a with corresponding image points $p_1, p_2 \in \mathbb{P}^2$ create the line $\ell = p_1 \times p_2$. We write the Euclidean intersection of the w axis with plane Π_a as $P_i = P_{w'} + \gamma_{\Pi_b}\hat{w}$ where Π_b :

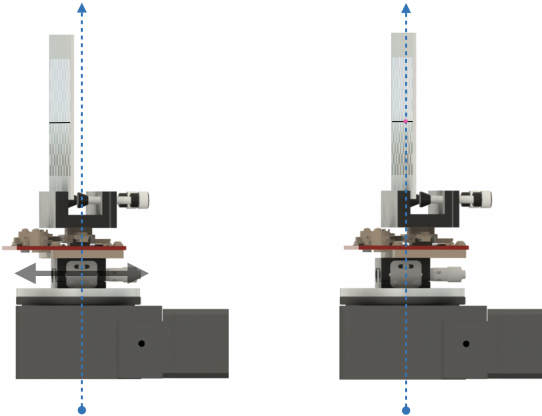


Figure 4.4: Sample motion assembly without sample mount

$\text{kernel}(\mathbf{P}_1, \mathbf{P}_2, \mathbf{P}_3)$ s.t. $\angle(\Pi_a, \Pi_b) = \pi/4$. Goal: Adjust compact stage position such that P_i lies on ℓ . This is true when $\mathbf{p}_i^\top \ell = 0$ in the image frame.

$$\hat{\mathbf{z}}' = \frac{(\mathbf{P}_2 - \mathbf{P}_1) \times (\mathbf{P}_3 - \mathbf{P}_1)}{\|(\mathbf{P}_2 - \mathbf{P}_1) \times (\mathbf{P}_3 - \mathbf{P}_1)\|} \quad (4.26)$$

$$\mathbf{p}_i = \tau \mathbf{M} \left((\boldsymbol{\alpha}^\top \hat{\mathbf{z}}') \delta + \hat{\mathbf{w}} (\mathbf{P}_1 - \mathbf{P}_{w'})^\top \hat{\mathbf{z}}' + \frac{1}{\tau} \mathbf{P}_{w'} \right) \quad (4.27)$$

where \mathbf{M} is the camera projection matrix, and $\tau = (\mathbf{w}^\top \hat{\mathbf{z}}')^{-1}$

$$\ell = \mathbf{M} \left((\boldsymbol{\alpha} \times \mathbf{P}_2 + \mathbf{P}_1 \times \boldsymbol{\alpha}) \delta + \mathbf{P}_1 \times \mathbf{P}_2 \right) \quad (4.28)$$

The signed PID alignment error is $\epsilon = \mathbf{p}_i^\top \ell$, and the loop is run until the error is less than a tenth of the thickness of the gene frame with a standard deviation of 0.05 mm across 20 measurements.

4.7 Aligning Sample Motion Assembly and Illumination Beams

The objectives for beam alignment are to orient the two laser beams such that their intersection point is located on the RT-3 and RT-5 rotation axes, and their mean direction is perpendicular to the rotation axes. This ensures that both beams' speckle images are generated from the same region in the sample and that the same region is sampled as we rotate the illuminators through the range of scattering angles.

Alignment proceeds as following. Given collinear azimuthal and RT-3 rotation axes, we can treat them as one axes with direction $\hat{\mathbf{h}}$ and location \mathbf{P}_h . This axis is located in the plane of a calibration target from previous alignment steps. For a beam spot a $\mathbf{Q}_{a_0} \in \mathbb{R}^3$ located on the plane, the displacement vector from the beam spot to the axis is $\Delta_0 = \mathbf{P}_h + \mathbf{d}_0 - (\mathbf{P}_h + \hat{\mathbf{h}} \mathbf{d}_0^\top \hat{\mathbf{h}})$. We use a PID controller to displace the beam by Δ_0 to within a tenth of the beam diameter. We repeat this for the second beam so both beam

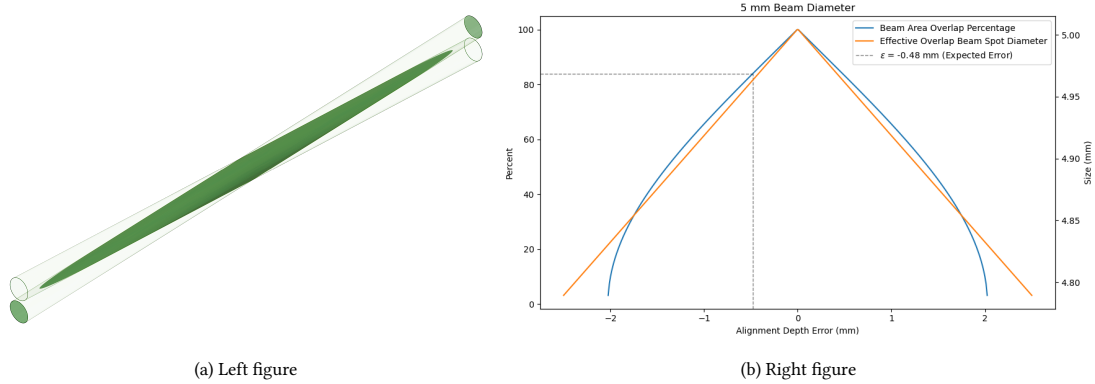


Figure 4.5: Combined figure

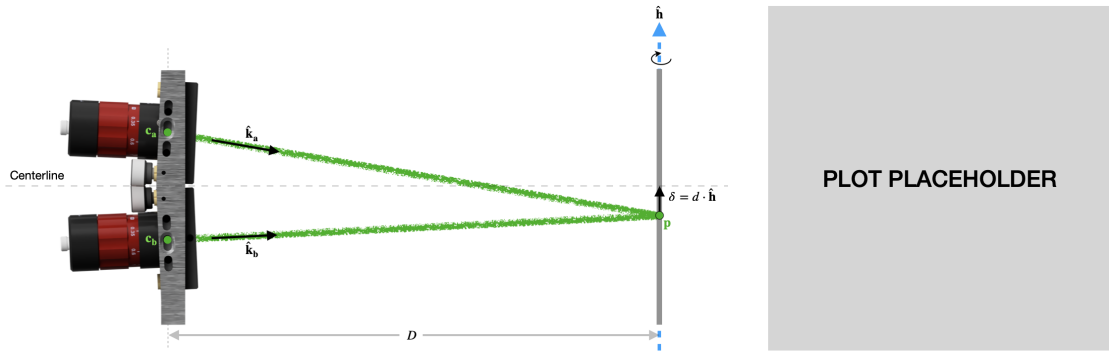


Figure 4.6

spots are located on the azimuthal axis. With beam spots a and b now located at Q_{a_1}, Q_{b_1} , we steer both beams to their mean position \bar{Q} so their intersection is located on the azimuthal axis.

$$\ell = 2 \frac{d_0}{\sin \theta} \cos \theta / 2 \quad (4.29)$$

$$d = 2 \frac{d_0}{\sin \theta} \sin (\theta / 2) \quad (4.30)$$

Both beams are equiangular with respect to the azimuthal axis when their projections onto the axis are equal and opposite.:

$$0 = \hat{\mathbf{k}}_a^\top \mathbf{h} + \hat{\mathbf{k}}_b^\top \mathbf{h}. \quad (4.31)$$

Define both beams' collimators positions c_a, c_b . The ideal intersection point Q^* is located at the intersection of the collimators' horizontal plane of symmetry and the azimuthal axis. \bar{Q} is offset from the ideal intersection point by displacement vector $\delta = Q^* - Q = d \cdot \hat{\mathbf{h}}$. Equation 4.31 can be rewritten in

terms of these variables to solve for the displacement distance d along $\hat{\mathbf{h}}$:

$$\begin{aligned} 0 &= (Q + \delta - c_a)^\top \hat{\mathbf{h}} + (Q + \delta - c_b)^\top \mathbf{h} \\ 2\delta^\top \hat{\mathbf{h}} &= (c_a - Q)^\top \hat{\mathbf{h}} + (c_b - Qp)^\top \mathbf{h} \\ 2\delta^\top \hat{\mathbf{h}} &= (c_a - Q + c_b - Q)^\top \hat{\mathbf{h}} \\ d \cdot \hat{\mathbf{h}}^\top \hat{\mathbf{h}} &= \frac{1}{2}(c_a - Q + c_b - Q)^\top \hat{\mathbf{h}} \\ d &= \frac{1}{2}[(c_a - Q) + (c_b - Q)]^\top \hat{\mathbf{h}} \end{aligned} \quad (4.32)$$

The displacement vectors $c_a - p$ and $c_b - Q$ are unknown since the collimator positions are unknown. However, the normalized beam directions $\hat{\mathbf{k}}_a, \hat{\mathbf{k}}_b$ are parallel to these displacement vectors, so we approximate a scaling coefficient s to achieve the correct scale. We determine s using the CAD model based on the nominal design geometry, and the final beam intersection displacement expression is

$$d = -\frac{s}{2}(\hat{\mathbf{k}}_a + \hat{\mathbf{k}}_b)^\top \hat{\mathbf{h}}. \quad (4.33)$$

The alignment procedure is as follows. Since the beams' orientations have been adjusted since their initial estimation, we begin by updating their estimates. We use a method similar to that detailed in section 4.3, but we use a single azimuthal position $\theta = 0$ rather than rotating the beam pair azimuthally. With update $\hat{\mathbf{k}}_a$ and $\hat{\mathbf{k}}_b$, and we compute the required intersection point displacement via Equation 4.33. The displacement is projected into the image frame, and the beams are commanded to the corresponding pixel backprojected to the calibration target. This process is repeated iteratively until the displacement distance is below a threshold due to the approximate scale factor s and other noise sources.

4.8 Aligning Calibration Target with Illumination Beams

This alignment step determines the "home" position of the sample assembly's rotation stage which corresponds to sample illumination along its normal vector. The home position maximizes the inner product of the target's normal vector and the mean illumination beam vector $\bar{\mathbf{k}} = (\hat{\mathbf{k}}_a + \hat{\mathbf{k}}_b)/2$.

4.9 Note: Proposal: Acquisition Camera Calibration

The projection matrix can be estimated via PnP in theory. However, we found it challenging in practice due to 3D points at infinity providing no depth information, and the geometry of a camera focused at infinity producing unstable estimates due to an effective coupling of the intrinsic parameters. Note: Add reasons they fail. Since the acquisition camera maps points from the plane at infinity to the image plane,

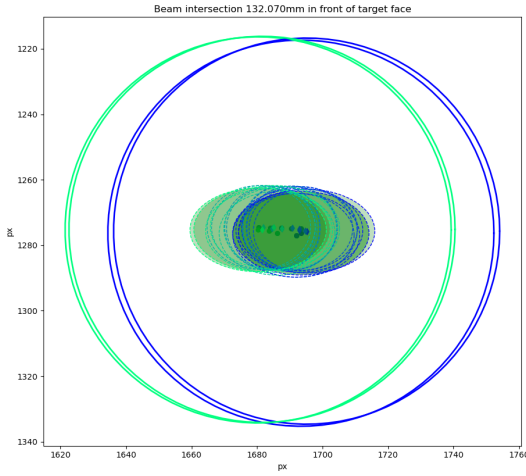


Figure 4.7

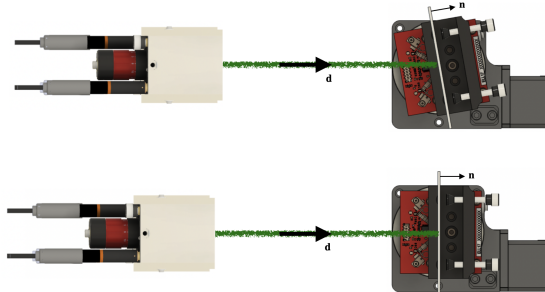


Figure 4.8: Top: Target and beam misaligned due to non-zero angle between the beam and the target normal; Bottom: d aligned with normal vector n . Note: Update by replacing d with $kbar$.

the homography for these planes is the projection matrix. However, there is an effective coupling of intrinsic parameters that complicates decomposing the projection matrix into a product of intrinsic and extrinsic matrices.

A camera focused at infinity maps rays along its optical axis to its principal point; all directions measured relative to the optical axis are mapped to image points relative to the principal point. Translating the principal point is similar to rotating the camera externally under the small angle approximation $\tan(\phi) \approx \phi$. Therefore, these two parameters are effectively coupled for a non-WFOV camera. Note: Insert figure showing reprojection error loss vs. pp and rotation. To avoid this issue, we estimate the focal length using a simple geometric relationship describing pinhole cameras focused at infinity followed principal point estimation via inspection. Once the intrinsics are known, we estimate the rotation matrix

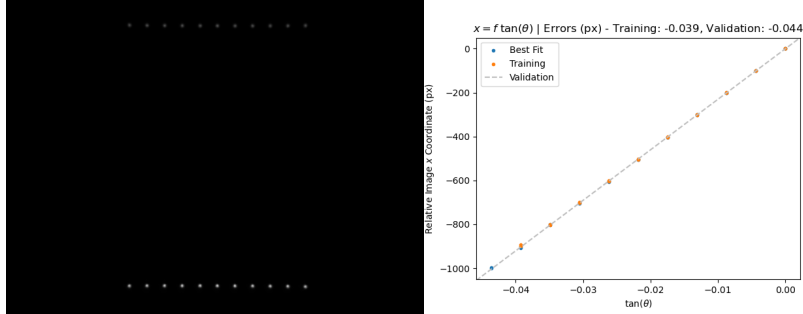


Figure 4.9: Left: Composite of 11 images of both illuminators spanning an azimuth range 3.5° . Right: The acquisition camera's focal length is the constant of proportionality of image point displacement and the tangent of the internal ray angle with respect to the optical axis.

and the lens distortion coefficients simultaneously.

4.9.1 Intrinsics

Rays entering the camera at an angle ϕ with respect to the optical axis are mapped to a point $f_{px} \tan(\phi)$ pixels from the principal point. This relation can be used to estimate the focal length given a set of rays with known directions and their corresponding image pixel coordinates. Since beam directions are known for all azimuth angles from lower stage calibration Note: Insert reference, we acquire images of beams rotated azimuthally, we compute the ray angle with respect to the optical axis and the pixel spacing. If we plot the pixel spacing vs. the tangent of the local ray angle, the line of best fit has a slope equal to the equivalent pinhole's focal length. We estimate the principal point by shining a collimated source into the lens oriented so it is approximately parallel to the lens' optical axis. The location of its image is assumed to be the principal point.

4.9.2 Extrinsics & Lens Distortion

Note: Newton-Raphson method via pytorch-minimize.

4.9.3 Validation

The calibration model is validated on the physical acquisition system by learning a model on training data and then evaluating performance via a validation dataset. First, a checkerboard calibration target is placed at two different locations, and its poses are determined using a calibrated camera. A laser is attached to a rotation stage, and an image of the beam spot on the target is acquired at each position. The 3D beam-plane intersection point is then calculated using beam spot centroiding to find the pixel

coordinates which are backprojected to the camera’s frame using the camera matrix. The rotation stage axis \mathbf{h} is determined by placing a target face-up on the stage and estimating the target’s normal with the camera.

Validation Results Figure 4.1d shows the training and validation estimation errors of 3D points. Angles less than 90° correspond to the target illuminated from the front with 0° corresponding to Figure 4.1c. Those to the right correspond to a back-illuminated target with 180° being anti-normal. The training and validation errors have similar trends with reduced validation error, suggesting the data was not over-fit. There is no error benchmark rooted in a performance metric. However, since centroiding and the homography computed during calibration both have sub-pixel accuracy and this is ultimately an interpolation task, the targeted prediction accuracy is sub-pixel. Considering the minimum validation error is 1.5 pixels with a mean error of 2.8 pixels, the targeted accuracy seems achievable if the issue of worsening error with angle of incidence is alleviated and the beam direction estimates are improved.

4.10 Note: Proposal: Illuminator Assembly Calibration

The goal for calibrating the illuminator assembly is estimating its rotation axis and the 3D orientation of the illumination beams as a function of the azimuth angle θ . We do so by computing the 3D intersection of each illumination beam with a series of N planes whose poses we know. This process is repeated for all $\theta \in \Theta$ for a total of $2N|\Theta|$ points. From this point set, we can estimate illumination directions for both beams as a function of θ and the azimuth stage pose up to a rotational ambiguity about its rotation axis.

Note: Proposal: Azimuth Stage Rotation Axis Each beam is associated with a set of $N|\Theta|$ points. Define a set of difference vectors $\{\tilde{\mathbf{k}}_\theta\}$, $|\{\tilde{\mathbf{k}}_\theta\}| = L$ as the differences between all N permute 2 points along a ray. We define a ray as a beam located at any particular $\theta \in \Theta$. Each $\tilde{\mathbf{k}}_\theta$ makes an angle $\pi/2 - \alpha$ with the rotation axis. However, the L_2 2nd order difference vectors are perpendicular to the azimuth rotation axis $\hat{\mathbf{h}}$, and we estimate $\hat{\mathbf{h}}$ as their null space.

Note: Proposal: Beam Direction Vector Once we know the azimuth rotation axis, we can use it to estimate both illuminators’ beam directions. For each $\theta \in \Theta$, we compute the centroid $\bar{\mathbf{p}}_\theta = \frac{1}{N} \sum \mathbf{p}_n$. We subtract the centroid from the point set so it is zero mean, and we rotate it about $\hat{\mathbf{h}}$ by $-\theta$ so all points are aligned with $\theta = 0$. The beam direction \mathbf{k}_0 is simply the point set’s principal component. For any arbitrary azimuthal angle θ , we can compute the beam direction $\mathbf{k}_0 = R_{\hat{\mathbf{h}}} \mathbf{k}_0$ where $R_{\hat{\mathbf{h}}}$ is a 3×3 rotation matrix with azimuthal axis $\hat{\mathbf{h}}$.

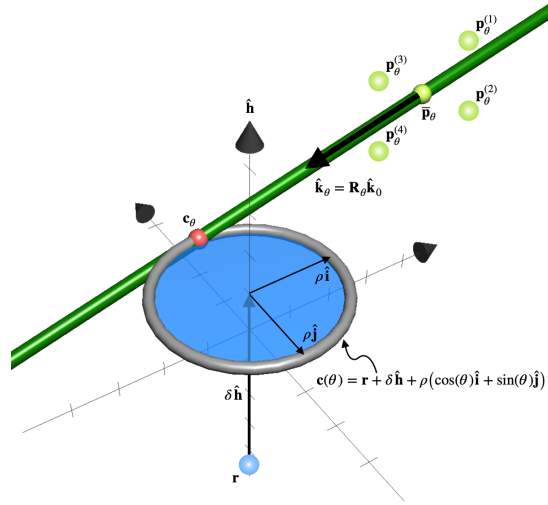


Figure 4.10: Ray envelope defined as the locus of points of closest encounter between the illumination beam and its rotation axis

4.10.1 Note: Proposal: Stage Position & Beam Direction as a Function of θ

Assume a collimated beam fixed to a rotation stage with location r and rotation axis \hat{h} . If the stage is rotated 360 degrees, the pencil of rays created by the rotated beam will form a paraboloid with axis \hat{h} and small radius ρ equal to the distance of closest encounter of the beam with the paraboloid axis. The locus of these points of closest encounter constitute the beam's ray envelope. The isoline of the ray envelope is

$$\mathbf{c}(\theta) = \mathbf{r} + \delta\hat{\mathbf{h}} + \mathbf{r}(\theta)\boldsymbol{\rho}_0, \quad (4.34)$$

where δ is the height of the circle above the stage, $\boldsymbol{\rho}$ is a 2×1 vector. $\mathbf{r}(\theta)$ is a 3×2 matrix consisting of a rotation of two basis vectors $\hat{\mathbf{i}}$ and $\hat{\mathbf{j}}$ through an angle of θ about the rotation axis $\hat{\mathbf{h}}$ with each basis vector being perpendicular to $\hat{\mathbf{h}}$

$$\mathbf{r}(\theta) = \mathbf{R}(\hat{\mathbf{h}}, \theta) \begin{bmatrix} \hat{\mathbf{i}} & \hat{\mathbf{j}} \end{bmatrix}, \quad \mathbf{R}(\hat{\mathbf{h}}, \theta) \in \mathbb{R}^{3 \times 3}. \quad (4.35)$$

If M points $\mathbf{p}_{\theta}^{(1)}, \mathbf{p}_{\theta}^{(2)}, \dots, \mathbf{p}_{\theta}^{(M)}$ are measured along the ray at a given rotation stage position $\theta \in \Theta$, then the beam with direction $\hat{\mathbf{k}}_{\theta}$ passes through their centroid $\bar{\mathbf{p}}_{\theta}$ with its pencil defined

$$\mathbf{l}_{\theta}(s) = \bar{\mathbf{p}}_{\theta} + s\hat{\mathbf{k}}_{\theta} \quad (4.36)$$

4.11 Acquisition Camera Calibration

The projection matrix can be estimated using PnP in theory. However, we found it challenging in practice due to 3-D points at infinity providing no depth information, resulting in unstable estimation. Since the

acquisition camera maps points from the plane at infinity to the image plane, the homography relating these planes is the projection matrix. However, there is an effective coupling of intrinsic and extrinsic parameters that complicates decomposing the projection matrix into a product of intrinsic and extrinsic matrices.

A camera focused at infinity maps rays parallel to its optical axis to its principal point; all directions measured relative to the optical axis are mapped to image points relative to the principal point. If p is the distance of a pixel from the principal point of a camera with focal length f , then $p = f \tan(\phi)$ for an incoming ray at angle θ with respect to the optical axis. Under the small angle approximation, $p \approx f\phi$ which means the pixel distance change proportionally to the incoming ray angle. Therefore, shifting the principal point is analogous to rotating the camera externally for small angles, and these two parameters are effectively coupled for a non-WFOV camera. This numerical coupling results in a reprojection error loss topology that is not strictly convex as shown in Figure 4.11(c). Therefore, we estimate the intrinsics by computing the focal length as the ambiguity's constant of proportionality and choosing a principal point. Once the intrinsics are known, we estimate the rotation matrix and the lens distortion coefficients simultaneously.

Since the focal length is the constant of proportionality for beam angle and image pixel displacement and the beam directions are known for all azimuth angles from illuminator assembly calibration, we can compute the focal length. We acquire images of the two illumination beams rotated azimuthally and compute ray angles with respect to the optical axis. If we plot the pixel spacing vs. the tangent of the local ray angle, the line of best fit has a slope equal to the equivalent pinhole camera's focal length (Figure 4.11(a,b)). We separately estimate the principal point by shining a collimated source into the lens oriented so it is approximately parallel to the lens' optical axis. The location of its image is assumed to be the principal point. Finally, we estimate the camera's rotation matrix and lens distortion coefficients numerically as the parameters that minimize the reprojection error given the previously determined focal length and principal point.

4.11.1 Beam Calibration

4.12 Note: Proposal:Acquisition Light Efficiency

Given a linearly polarized illumination laser beam, an acquisition sensor offset by a scattering angle θ , and a scattering sample inside a glass cell, the goal is to determine 1) the optimal sample orientation and 2) the optimal angle of polarization to maximize light transmitted from the illuminator to the acquisition

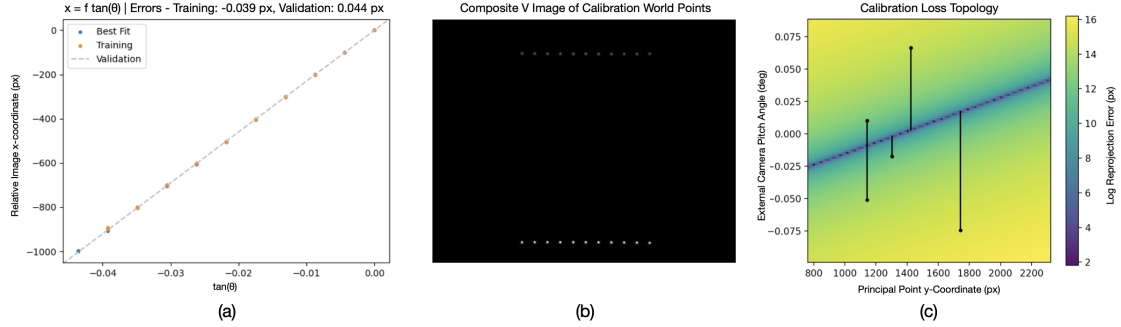


Figure 4.11: (a) The acquisition camera's focal length is the constant of proportionality of image point displacement and the tangent of the internal ray angle with respect to the optical axis; (b) Composite of 11 images of both illuminators spanning an azimuth range 3.5° ; (c) Reprojection error as a function of principal point shifts along the y-axis and external pitch rotation is not strictly convex, showing the numerical ambiguity of principal point shifting and camera rotation. This ambiguity holds for the x-axis and panning as well.

sensor. All theory below assumes scattering particles are small compared with the wavelength and are detailed in [8].

Note: Proposal:Fresnel Formulae

Consider a plane wave with amplitude A incident on a surface. The electric and magnetic field vectors can be decomposed into two components parallel and perpendicular to the surface plane. The incident electric field is

$$E^{(i)} = \begin{bmatrix} -A_{||} \cos \theta_i e^{-i\tau_i} \\ A_{\perp} e^{-i\tau_i} \\ A_{||} \sin \theta_i e^{-i\tau_i} \end{bmatrix} \quad (4.37)$$

where E_x, E_z are in the plane, E_y is along the plane normal, and the complex exponential argument is defined

$$\tau_i = \omega \left(t - \frac{\mathbf{r}^\top \mathbf{s}^{(i)}}{v} \right) = \omega \left(t - \frac{x \sin \theta_i + z \cos \theta_i}{v} \right). \quad (4.38)$$

The magnetic field vector H is written similarly through the relation $H = \sqrt{\epsilon} \mathbf{s} \times \mathbf{E}$. where \mathbf{s} is the light's velocity vector. If T and R denote the transmitted and reflected amplitudes, then the transmitted field is

$$E^{(t)} = \begin{bmatrix} -T_{||} \cos \theta_t e^{-i\tau_t} \\ T_{\perp} e^{-i\tau_t} \\ T_{||} \sin \theta_t e^{-i\tau_t} \end{bmatrix}, \quad (4.39)$$

and the reflected field is

$$\mathbf{E}^{(r)} = \begin{bmatrix} -R_{||} \cos \theta_r e^{-i\tau_r} \\ R_{\perp} e^{-i\tau_r} \\ R_{||} \sin \theta_r e^{-i\tau_r} \end{bmatrix}. \quad (4.40)$$

The tangential components of the electric and magnetic fields must be continuous across the boundary, resulting in four boundary conditions:

$$E_x^{(i)} + E_x^{(r)} = E_x^{(t)} \quad E_y^{(i)} + E_y^{(r)} = E_y^{(t)} \quad (4.41)$$

$$H_x^{(i)} + H_x^{(r)} = H_x^{(t)} \quad H_y^{(i)} + H_y^{(r)} = H_y^{(t)}. \quad (4.42)$$

These boundary conditions can be solved for an expression of the transmitted and reflected amplitudes components by using the Maxwell relation $n = \sqrt{\epsilon}$

$$T_{||} = \frac{2n_1 \cos \theta_i}{n_2 \cos \theta_i + n_1 \cos \theta_t} A_{||} \quad T_{\perp} = \frac{2n_1 \cos \theta_i}{n_1 \cos \theta_i + n_2 \cos \theta_t} A_{\perp} \quad (4.43)$$

$$R_{||} = \frac{n_2 \cos \theta_i - n_1 \cos \theta_t}{n_2 \cos \theta_i + n_1 \cos \theta_t} A_{||} \quad R_{\perp} = \frac{n_1 \cos \theta_i - n_2 \cos \theta_t}{n_1 \cos \theta_i + n_2 \cos \theta_t} A_{\perp}. \quad (4.44)$$

Note: Proposal:Effects of Polarization on Fresnel Formulae

The light intensity is

$$S = \frac{c}{4\pi} \sqrt{\epsilon} E^2 = \frac{cn}{4\pi} E^2 \quad (4.45)$$

The resulting energy incident on a surface with unit area A is

$$J^{(i)} = S^{(i)} \cos \theta_i = \frac{cn_1}{4\pi} |A|^2 \cos \theta_i \quad (4.46)$$

with reflected and transmitted energies

$$J^{(r)} = \frac{cn_1}{4\pi} |R|^2 \cos \theta_i \quad \text{and} \quad J^{(t)} = \frac{cn_2}{4\pi} |T|^2 \cos \theta_t. \quad (4.47)$$

The reflectivity and transmissivity are

$$\mathcal{R} = \frac{J^{(r)}}{J^{(i)}} = \frac{|R|^2}{|A|^2} \quad \text{and} \quad \mathcal{T} = \frac{J^{(t)}}{J^{(i)}} = \frac{|T|^2}{|A|^2} \quad (4.48)$$

which satisfy the law of conservation of energy by summing to 1

$$\mathcal{R} + \mathcal{T} = 1. \quad (4.49)$$

The reflectivity and transmissivity are functions of polarization with respect to the parallel and perpendicular directions. If the incident electric field \mathbf{E} makes an angle α_i with respect to the plane, the parallel and perpendicular area components are

$$A_{||} = A \cos \alpha_i \quad \text{and} \quad A_{\perp} = A \sin \alpha_i \quad (4.50)$$

The parallel energy component of the incident light is

$$\begin{aligned} J_{||}^{(i)} &= \frac{cn_1}{4\pi} |A_{||}|^2 \cos \theta_i \\ &= \frac{cn_1}{4\pi} |A|^2 \cos^2 \alpha_i \cos \theta_i \\ &= J^{(i)} \cos^2 \alpha_i \end{aligned} \quad (4.51)$$

with that of the perpendicular component following similarly:

$$J_{\perp}^{(i)} = J^{(i)} \sin^2 \alpha_i. \quad (4.52)$$

The reflectivity in terms of polarized light is

$$\begin{aligned} \mathcal{R} &= \frac{J^{(r)}}{J^{(i)}} = \frac{J_{||}^{(r)} + J_{\perp}^{(r)}}{J^{(i)}} \\ &= \frac{J_{||}^{(r)}}{J_{||}^{(i)}} \cos^2 \alpha_i + \frac{J_{\perp}^{(r)}}{J_{\perp}^{(i)}} \sin^2 \alpha_i \\ &= \mathcal{R}_{||} \cos^2 \alpha_i + \mathcal{R}_{\perp} \sin^2 \alpha_i, \end{aligned} \quad (4.53)$$

and the transmissivity is

$$\mathcal{T} = \mathcal{T}_{||} \cos^2 \alpha_i + \mathcal{T}_{\perp} \sin^2 \alpha_i. \quad (4.54)$$

Reflectivity and transmissivity must satisfy conservation of energy respectively:

$$\mathcal{R}_{||} + \mathcal{T}_{||} = 1, \quad \mathcal{R}_{\perp} + \mathcal{T}_{\perp} = 1. \quad (4.55)$$

When light is incident normal to the surface, $\alpha_i = 0$ for all E-field orientations, meaning there is no distinction between the parallel and perpendicular components, and the reflectivity and transmissivity are written

$$\mathcal{R} = \left(\frac{n - 1}{n + 1} \right)^2, \quad \mathcal{T} = \frac{4n}{(n + 1)^2} \quad (4.56)$$

where $n = n_2/n_1$.

These relations were used to find the optimal sample assembly rotation angle and the angle of polarization for every acquisition scattering angle. The result is a lookup table plotted as a chart in Figure 4.12.

4.13 Note: Proposal:Expected Results

We have identified imaging configurations that produce high-contrast speckle images with well-resolved speckle grains through HDR acquisition and proper camera specifications. Examples of images we have

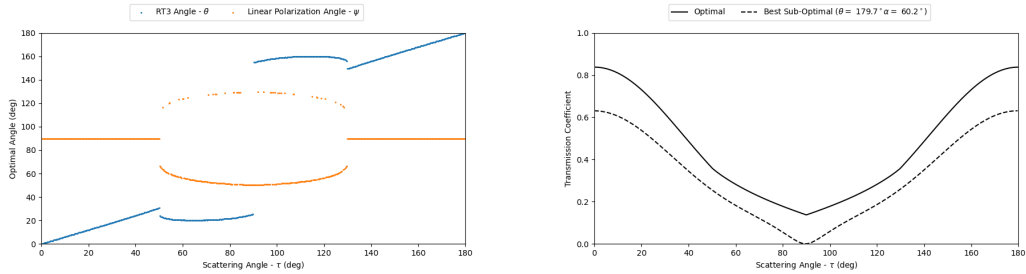


Figure 4.12: Left: Optimal sample rotation stage position and linear polarization angle as a function of azimuthal illumination angle. The linear polarization angle schedule contains discontinuities in the range $(-50^\circ, 50^\circ)$ due to rounding errors; Right: Comparison of light transmitted towards camera when choosing the optimal sample orientation versus a static sample shows an approximate 15% increase on average.

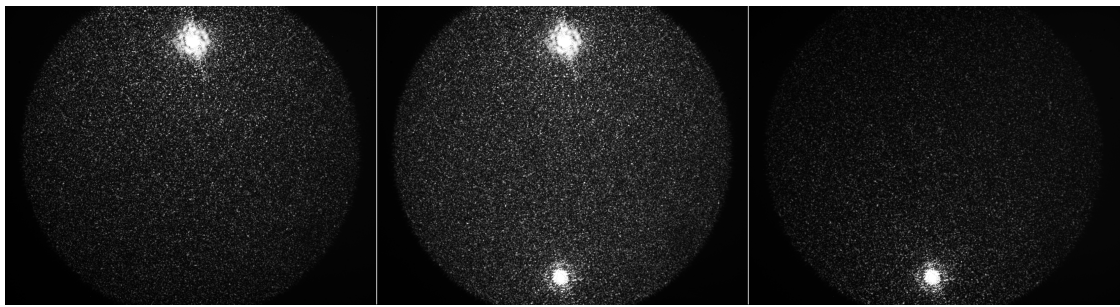


Figure 4.13: Speckle images of $10\mu\text{m}$ monodisperse SiO_2 beads acquired using scatterometer setup. Left: Top illuminator activated; Center: Both illuminators activated; Right: Bottom illuminator activated

acquired to date are shown in Figure 4.13. These speckle images are high-contrast which is indicative of a suitable beamwidth (5mm) for the sample's scattering cross-section, and the speckle grains are well-resolved, meaning the camera's angular resolution is sufficient.

A preliminary result that indicates we are on the right track is computing and plotting 2D speckle correlation and showing that this correlation increases with decreasing sample optical density. Next, we plan to acquire phase functions of materials similar those acquired in [1] over a larger range of scattering angles. Figure 4.14 shows our planned extension of the scattering angle range. If our phase functions agree with [1], it will help validate our acquisition configuration and correlation scripts.

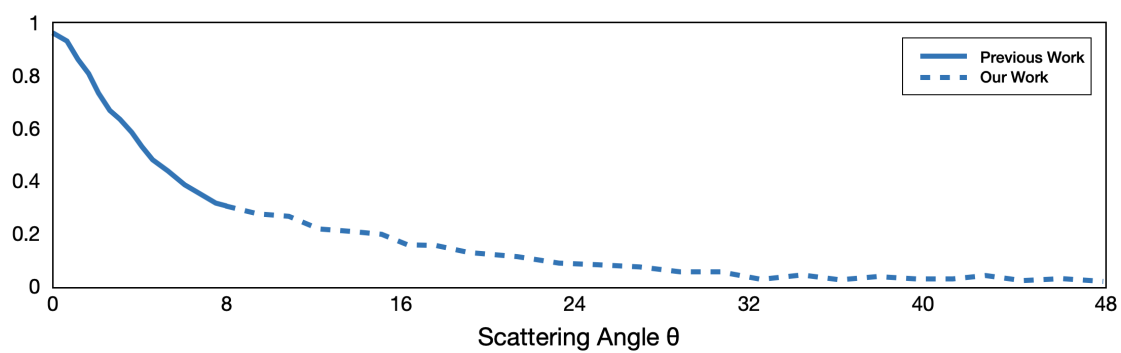


Figure 4.14: An expected result is acquiring the scattering phase function for a larger range of scattering angles than the literature.

Chapter 5

Scattering Sample Preparation

In this chapter, we detail the process for preparing scattering samples for scatterometer acquisition. We also discuss characterization methods used to determine the optical properties of samples necessary for the single scattering approximation and to compute the scattering phase function.

5.0.1 Equipment

- Microscope slide - Menzel Glaser SUPERFROST Frosted End (no. 12-550-15)
- Cover glass - Corning 24x50 mm (no. 2975-245)
- Gene frame 125 μL - Thermo Scientific (no. AB0578)
- Low melt temperature agarose - RPI (no. 9012-36-6)
- DI(?) water
- 10 μm silica monodisperse, non-porous - Sigma-Aldrich (no. 904368)
- 15 mL centrifuge tube
- Pipette set to 125 μL intake
- Isopropyl alcohol
- Centrifuge tube heater - Ohaus 2 block dry block heater (no. HB2DG)
- mg Scale

5.0.2 Procedure

1. Pour 5 mL DI(?) water into a 15 mL centrifuge tube (tube #1) and a 10 mL tube (tube #2)
2. Cut a clean pipette tip so its opening is 2-3mm in diameter.
3. Place the pipette tip inside tube #2. Its wide tip should be above the water's surface.
4. Heat both tubes to 100 °C
5. While the tubes are heating, place the microscope slide on the border of the heater
6. Create 1% agarose solution by adding 50 mg agarose powder to centrifuge tube #1 (see Equation)
7. Shake centrifuge tube 1 periodically until agarose is fully dissolved
8. For an OD 1 sample, add ____ mg silica monodisperse to tube #1(see Equation)
9. Heat the solution for 5 minutes, shaking periodically.
10. While the solution is heating, carefully remove the hot microscope slide from the heater. Remove one of the gene frame laminates, and adhere the gene frame on the slide so it is centered vertically and horizontally. The warm slide improves gene frame adhesion and promotes a better seal.
11. Place the slide and the cover glass in the center of the work area. Let the slide cool to room temperature. We found that depositing liquid onto a hot slide increases bead mobility and causes them to fall to the bottom of the gene frame.
12. Attach the heated pipette tip in tube #2 to the pipette.
13. With the centrifuge in the heating block, place the pipette tip at the bottom of the centrifuge tube and use the plunger to repeatedly cycle liquid in and out of the pipette tube. The turbulence disturbs beads that have fallen to the bottom of the tube and creates a more uniform concentration.
14. Slightly raise the tip from the bottom to avoid an air seal, and slowly press the plunger and slowly release it as you raise the tip from the bottom of the tube to the surface of the liquid. The plunger should be fully released before the tip reaches the surface to ensure there is no air intake.
15. In quick succession:
16. a) Place the pipette tip against the surface of the microscope slide, and dispense the liquid into the gene frame by pressing the plunger to its second stop. Remove the pipette from the liquid before releasing the plunger.

-
- b) Apply the cover glass from one of its long ends to the other to avoid air bubbles. It may be helpful to slide a smooth, small cylindrical bottle across the cover glass as you apply it to provide additional pressure.

5.0.3 Sample Characterization

Chapter 6

Acquisition

In this chapter, we delve into the scatterometer design as well as the calibration and alignment process.

6.1 Scattering Samples

6.2 Acquisition

6.3 Maximizing Light Scattered Towards Camera

6.3.1 Optimizing Illumination & Sample Orientation to Maximize Light Transmission

Given a linearly polarized illumination laser beam, an acquisition sensor offset by some scattering angle, and a scattering sample inside a glass cell, the goal is to determine 1) the optimal sample orientation and 2) the optimal angle of polarization to maximize light transmitted from the illuminator to the acquisition sensor.

Fresnel Formulae

The contents in this section are paraphrased from [8]. Consider a plane wave with amplitude A incident on a surface. The electric and magnetic field vectors can be decomposed into two components parallel and perpendicular to the surface plane. The incident electric field is

$$E^{(i)} = \begin{bmatrix} -A_{||} \cos \theta_i e^{-i\tau_i} \\ A_{\perp} e^{-i\tau_i} \\ A_{||} \sin \theta_i e^{-i\tau_i} \end{bmatrix} \quad (6.1)$$

where E_x, E_z are in the plane, and E_y is along the plane normal. The complex exponential argument is defined

$$\tau_i = \omega \left(t - \frac{\mathbf{r}^T \mathbf{s}^{(i)}}{v} \right) = \omega \left(t - \frac{x \sin \theta_i + z \cos \theta_i}{v} \right) \quad (6.2)$$

The magnetic field vector H is written similarly through the relation $H = \sqrt{\epsilon} \mathbf{s} \times \mathbf{E}$. where \mathbf{s} is the light's velocity vector. If T and R denote the transmitted and reflected amplitudes, then the transmitted field is

$$E^{(t)} = \begin{bmatrix} -T_{||} \cos \theta_t e^{-i\tau_t} \\ T_{\perp} e^{-i\tau_t} \\ T_{||} \sin \theta_t e^{-i\tau_t} \end{bmatrix}, \quad (6.3)$$

and the reflected field is

$$E^{(r)} = \begin{bmatrix} -R_{||} \cos \theta_r e^{-i\tau_r} \\ R_{\perp} e^{-i\tau_r} \\ R_{||} \sin \theta_r e^{-i\tau_r} \end{bmatrix}. \quad (6.4)$$

The tangential components of the electric and magnetic fields must be continuous across the boundary, resulting in four boundary conditions:

$$E_x^{(i)} + E_x^{(r)} = E_x^{(t)} \quad E_y^{(i)} + E_y^{(r)} = E_y^{(t)} \quad (6.5)$$

$$H_x^{(i)} + H_x^{(r)} = H_x^{(t)} \quad H_y^{(i)} + H_y^{(r)} = H_y^{(t)} \quad (6.6)$$

These boundary conditions can be solved for an expression of the transmitted and reflected amplitudes components by using the Maxwell relation $n = \sqrt{\epsilon}$

$$T_{||} = \frac{2n_1 \cos \theta_i}{n_2 \cos \theta_i + n_1 \cos \theta_t} A_{||} \quad T_{\perp} = \frac{2n_1 \cos \theta_i}{n_1 \cos \theta_i + n_2 \cos \theta_t} A_{\perp} \quad (6.7)$$

$$R_{||} = \frac{n_2 \cos \theta_i - n_1 \cos \theta_t}{n_2 \cos \theta_i + n_1 \cos \theta_t} A_{||} \quad R_{\perp} = \frac{n_1 \cos \theta_i - n_2 \cos \theta_t}{n_1 \cos \theta_i + n_2 \cos \theta_t} A_{\perp} \quad (6.8)$$

Effects of Polarization on Fresnel Formulae

The light intensity is

$$S = \frac{c}{4\pi} \sqrt{\epsilon} E^2 = \frac{cn}{4\pi} E^2 \quad (6.9)$$

The resulting energy incident on a surface with unit area A is

$$J^{(i)} = S^{(i)} \cos \theta_i = \frac{cn_1}{4\pi} |A|^2 \cos \theta_i \quad (6.10)$$

with reflected and transmitted energies

$$J^{(r)} = \frac{cn_1}{4\pi} |R|^2 \cos \theta_i \quad \text{and} \quad J^{(t)} = \frac{cn_2}{4\pi} |T|^2 \cos \theta_t. \quad (6.11)$$

The reflectivity and transmissivity are

$$\mathcal{R} = \frac{J^{(r)}}{J^{(i)}} = \frac{|R|^2}{|A|^2} \quad \text{and} \quad \mathcal{T} = \frac{J^{(t)}}{J^{(i)}} = \frac{|T|^2}{|A|^2} \quad (6.12)$$

which satisfy the law of conservation of energy by summing to 1

$$\mathcal{R} + \mathcal{T} = 1. \quad (6.13)$$

The reflectivity and transmissivity are functions of polarization with respect to the parallel and perpendicular directions. If the incident electric field E makes an angle α_i with respect to the plane, the parallel and perpendicular area components are

$$A_{||} = A \cos \alpha_i \quad \text{and} \quad A_{\perp} = A \sin \alpha_i \quad (6.14)$$

The parallel energy component of the incident light is

$$\begin{aligned} J_{||}^{(i)} &= \frac{cn_1}{4\pi} |A_{||}|^2 \cos \theta_i \\ &= \frac{cn_1}{4\pi} |A|^2 \cos^2 \alpha_i \cos \theta_i \\ &= J^{(i)} \cos^2 \alpha_i \end{aligned} \quad (6.15)$$

with that of the perpendicular component following similarly:

$$J_{\perp}^{(i)} = J^{(i)} \sin^2 \alpha_i. \quad (6.16)$$

The reflectivity in terms of polarized light is

$$\begin{aligned} \mathcal{R} &= \frac{J^{(r)}}{J^{(i)}} = \frac{J_{||}^{(r)} + J_{\perp}^{(r)}}{J^{(i)}} \\ &= \frac{J_{||}^{(r)}}{J_{||}^{(i)}} \cos^2 \alpha_i + \frac{J_{\perp}^{(r)}}{J_{\perp}^{(i)}} \sin^2 \alpha_i \\ &= \mathcal{R}_{||} \cos^2 \alpha_i + \mathcal{R}_{\perp} \sin^2 \alpha_i, \end{aligned} \quad (6.17)$$

and the transmissivity is

$$\mathcal{T} = \mathcal{T}_{||} \cos^2 \alpha_i + \mathcal{T}_{\perp} \sin^2 \alpha_i. \quad (6.18)$$

Reflectivity and transmissivity must satisfy conservation of energy respectively:

$$\mathcal{R}_{||} + \mathcal{T}_{||} = 1, \quad \mathcal{R}_{\perp} + \mathcal{T}_{\perp} = 1. \quad (6.19)$$

When light is incident normal to the surface, $\alpha_i = 0$ for all E-field orientations, meaning there is no distinction between the parallel and perpendicular components, and the reflectivity and transmissivity are written

$$\mathcal{R} = \left(\frac{n - 1}{n + 1} \right)^2, \quad \mathcal{T} = \frac{4n}{(n + 1)^2} \quad (6.20)$$

where $n = n_2/n_1$.

Fresnel Relations as Mueller Matrices

Transmission

Scattering This section summarizes the results in [7]. Assuming light with wavevector k is scattered from a small sphere with radius a with scattering amplitude coefficient $a_1 \in \mathbb{C}$, the scattered field at distance r from the scatterer, the Mueller matrix is

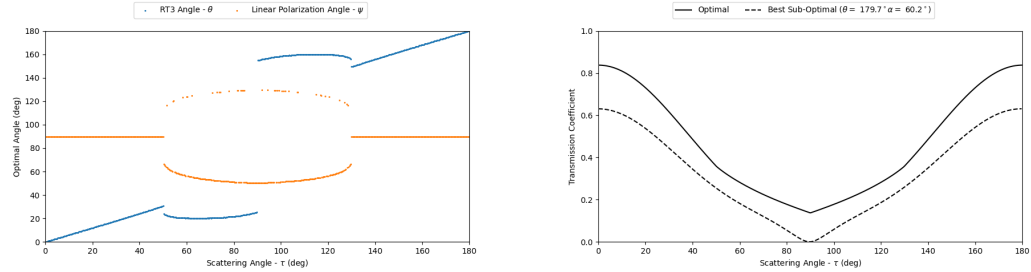


Figure 6.1

$$\mathbf{M}_s = \frac{9|a_1|^2}{4k^2r^2} \begin{bmatrix} \frac{1}{2}(1 + \cos^2 \theta) & \frac{1}{2}(\cos^2 \theta - 1) & 0 & 0 \\ \frac{1}{2}(\cos^2 \theta - 1) & \frac{1}{2}(1 + \cos^2 \theta) & 0 & 0 \\ 0 & 0 & \cos \theta & 0 \\ 0 & 0 & 0 & \cos \theta \end{bmatrix} \quad (6.21)$$

where the scattering coefficient is defined

$$a_1 = -\frac{i2x^3}{e} \frac{m^2 - 1}{m^2 + 2} - \frac{i2x^5}{5} \frac{(m^2 - 2)(m^2 - 1)}{(m^2 + 2)^2} \quad (6.22)$$

with scale factor and relative refractive index

$$x = ka = \frac{2\pi Na}{\lambda}, \quad m = \frac{N_1}{N} = \frac{k_1}{k} \quad (6.23)$$

where N and N_1 are the medium's and particle's refractive indices respectively. The scattering Mueller matrix is defined within the scattering plane containing the incoming and outgoing directions as well as the scattering particle.

Simulation Results

Unpolarized Beam

Linearly Polarized Beam

6.3.2 Simulation

6.3.3 Depolarizer Spatial Characterization

One option is to depolarize the illumination beams via Thorlabs DPP25-A liquid crystal polymer depolarizer. This optic is a series of linear polarizing strips each oriented in 45-degree increments. The incident

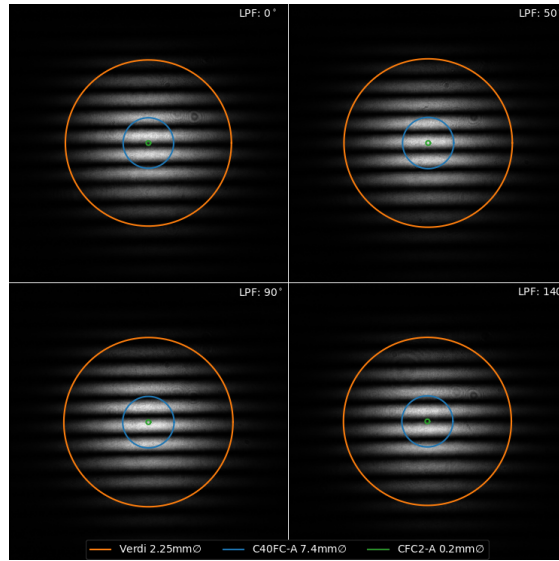


Figure 6.2

beam is passed through these strips, and the output beam is a combination of linear polarization states with different angles of polarization. Since strips are distributed spatially, the output beam's polarization state is a function of the incident beam size.

The effect of beam size on output polarization state was characterized by measuring the spatial distribution of polarization state using a camera. The Verdi output beam was coupled into a 2-meter single-mode fiber whose output was collimated using Thorlabs C40FC-A. That beam was passed through the depolarizer mounted on Thorlabs CRM1PT followed by a linear polarizing filter mounted on Thorlabs CRM1T. The beam was then passed through an ND=2.0 filter prior to measurement by the camera. The camera was Grasshopper3 GS3-PGE-91S6M with a Leica Summicron-A 50mm 1:2 lens focused at its shortest working distance (1:6.6 magnification). Acquisition consisted of rotating the LPF in 10-degree increments over a range of 170 degrees and acquiring a 16-bit image for each LPF orientation.

The intensity profiles of the depolarized beam for four LPF orientations is shown in Figure 6.2. Each profile is a Gaussian-enveloped sinusoid whose phase changes with the LPF orientation. Each image is overlaid with $1/e^2$ beam diameters for two collimators' output beams and the Verdi output beam. The C40FC-A and Verdi beam profiles are large enough to cover at least a full period of the depolarizer's structure, while the CFC2-A beam does not. Therefore, the depolarizer would not be effective if used with the CFC2-A collimator.

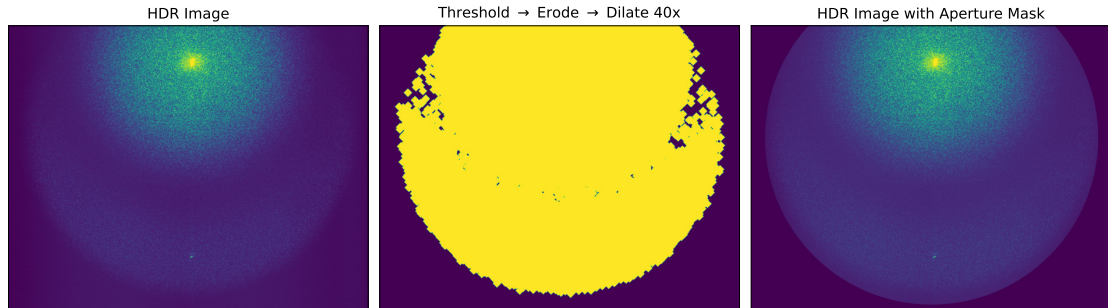
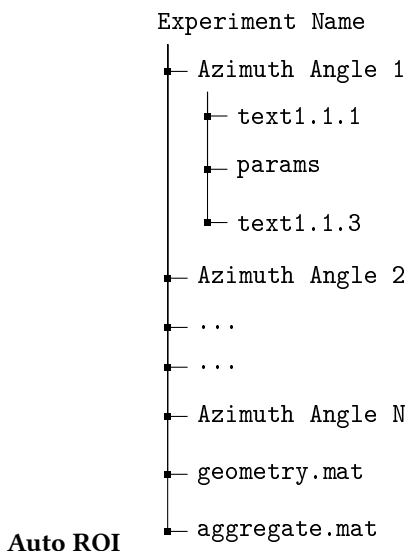


Figure 6.3

6.3.4 Data Processing



Chapter 7

Appendices

7.1 Calibration Target Design

A contiguous calibration target was chosen initially for beam direction estimation. However, the variable albedo due to ink created structured noise. This caused estimates of beams partially overlapping black regions to become biased towards the white regions. As a result, a window was added to the target allowing all centroiding estimates to occur on a surface of constant albedo. See Figure 7.1.

- Include info from WeeklyTagUp archive on checkerboard sizes
- Include square_size excel spreadsheet saved in data/Meetings/10-12-2025 on Dropbox

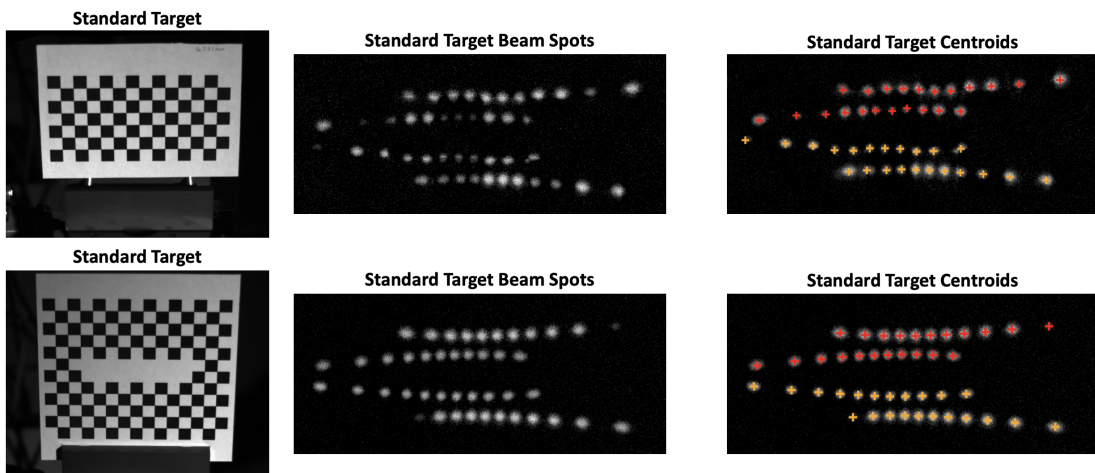


Figure 7.1: Top row: Original target used for calibration caused irregular beam spot shapes which produced noisy centroids. Bottom row: Windowed target used now to avoid albedo issues when imaging beam spots.

7.2 Reference Camera Lens Selection

7.3 Sample Preparation

Equipment Required

- Microscope slides (two per sample)
 - Dropper or syringe with capacity greater than or equal to the target sample volume
 - Ethanol
 - Isopropyl alcohol
 - Non-abrasive working surface to prevent scratching slides
1. Clean all labware with IPA and dry with Kimtech wipes. Clean slides with IPA and dry with optical cleaning cloth.
 2. Pour 5 mL HPLC water in a 15 mL tube using a squeeze bottle.
 3. Set the tube heater to 95°C and place the 15 mL tube in a heating block.
 4. Once the heater has reach the set point, place a clean 5 mL tube in a heating block. Let both tubes remain in the block for 5 minutes.
 5. Cut _ mm off the end of a clean pipette tip so its opening is 2 mm in diameter.
 6. Transfer heated HPLC water from the 15 mL tube to the 5 mL tube.
 7. Measure _ mg agarose powder in a clean weighting boat and add it to the 5 mL tube. Place it in a heating block for 10 minutes, using bottoms-up agitation every 2 minutes.
 8. While waiting, measure _ mg silica beads in the weigh boat and set aside.
 9. Attach a gene frame to a microscope slide.
 10. Once the water has been heated for 10 minutes, place the slide on a heating block. Then add the silica beads to the agarose solution and let the suspension heat for 5 minutes, using bottoms-up agitation every minute.
 11. Using a 1 mL pipette, cycle the liquid within the 5 mL tube several times.

12. Ensure the pipette's volume is set to 96% of the gene frame's volume.

Note: The following sequence should occur quickly. Otherwise the suspension will cool and begin gelling, reducing the sample quality:

13. Using heat-resistant gloves, remove the heated slide and place it on a microfiber towel.
14. Intake the desired volume of the suspension and aliquot it while moving the pipette tip across the area of the gene frame. This will minimize the height of the liquid and will prevent overflow when placing the slide cover on the gene frame.
15. Using another microscope slides, attach the slide cover from one side to another, lengthwise along the gene frame.
16. Press the slide flat against the slide cover and leave it in place to ensure the cover is parallel with the surface of the sample slide.
17. Weigh-out the amount using a scooper and clean weigh boat
18. Combine microspheres with _ mL ethanol in a centrifuge tube
 - Micro sphere volume: $14.137 \mu\text{m}^3 = 1.4137 \times 10^{-11} \text{cm}^3$
 - Micro spheres per gram: $3.1 \times 10^{11} \frac{\text{sphere}}{\text{g}} = \frac{1 \text{cm}^3}{2.196 \text{g}} \left(\frac{10^4 \mu\text{m}}{1 \text{cm}} \right)^3 \frac{1}{(\frac{4}{3}\pi 1.5^3) \mu\text{m}^3}$
 - Ethanol Volume: $\frac{3.1 \times 10^{11} \text{spheres}}{1 \text{g}} \cdot \frac{1.4137 \times 10^{-11} \text{cm}^3}{1 \text{sphere}} \cdot \frac{1 \text{mL}}{1 \text{cm}^3} \cdot 125 \cdot x \text{ grams}$
19. Measure-out 0.1 g of agarose powder and place in second tube
20. Fill second tube with 10 mL HPCL water
21. Fill 10 tubes with HPCL water
22. Insert all 12 tubes in heating block
23. Set the mixer to _ degrees Celsius and begin heating the tubes.
24. After _ minutes, start mixing the tubes at _ RPM for _ minutes.
25. Once done, pour the water tubes into a TBD container and place the slides in the water.
26. Pour the microsphere-Ethanol mixture into the agarose mixture and resume mixing and heating for _ minutes (depending on time required to heat-up slides).

27. Remove slides, dry them, attach gene frames, and place on non-abrasive surface. The next few steps should be completed quickly to avoid the slides cooling too much.
28. When mixing is complete, remove tube and agitate 20 times using the bottoms-up method
29. Place the mixture back in the mixer and use a pipette to transfer liquid to the center of the gene frame. The amount transferred should match the volume of the gene frame.
30. Sandwich the sample using the top face of another microscope slide (not the side that was facing down on the table). While sandwiching, touch the slides as far away from the gene frame as possible, and on the edges.
31. Place on the rotator at _ RPM for _ minutes (need to calculate cooling rate). The liquid and slides should now be at a uniform temperature.
32. Inspect the sample using a microscope objective to determine the uniformity. Need to develop procedure for this. Maybe 8 locations (3 along top, 3 along bottom, two intermediate positions along sample center line). Then compute variance of number of particles visible across images? Use that as a benchmark.
33. Clean pipette internals, glassware using IPA

7.4 Ziegler-Nichols Tuning Method

The Ziegler-Nichols tuning method is a PID tuning heuristic based on two principal characteristics affecting process controllability [42]:

1. The ultimate gain K_u is the proportional gain above which oscillations will increase to a maximum amplitude, and below which oscillations will decay to zero response.
2. The period of oscillation T_u is the period in minutes of constant-amplitude oscillations corresponding to a P controller with gain K_u .

It defines the necessary proportional (K_p), integral (K_i), and derivative (K_d) gains for control stability given the ultimate gain and period of oscillation.

Note: Alternative is Tyreus-Luyben method [25] For example, assume the error is directly proportional to the actuation distance of a translation stage. If the initial

Table 7.1: Ziegler-Nichols method

Control Type	K_p	T_i	T_d	K_i	K_d
P	$0.5 K_u$	-	-	-	-
PI	$0.45 K_u$	$0.83 T_u$	-	$0.54 K_u/T_u$	-
PD	$0.3 K_u$	-	$0.125 T_u$	-	$0.10 K_u T_u$
classic PID	$0.6 K_u$	$0.5 T_u$	$0.125 T_u$	$1.2 K_u/T_u$	$0.075 K_u T_u$
Pessen Integral Rule	$0.7 K_u$	$0.4 T_u$	$0.15 T_u$	$1.75 K_u/T_u$	$0.105 K_u T_u$
some overshoot	$0.33 K_u$	$0.50 T_u$	$0.33 T_u$	$0.66 K_u/T_u$	$0.11 K_u T_u$
no overshoot	$0.20 K_u$	$0.50 T_u$	$0.33 T_u$	$0.40 K_u/T_u$	$0.066 K_u T_u$

7.5 Parts Lists

7.6 Thin lens model validation: macro lenses

7.7 Technical drawings

Table 7.2: Parts List - Scatterometer Support Equipment

Description	Model/Part No.	Vendor	Qty.
Nexus Breadboard, 36" x 48" x 2.4"	B3648F	Thorlabs	1
Aluminum Breadboard 12" x 24" x 1/2"	MB1224	Thorlabs	1
Aluminum Breadboard 12" x 18" x 1/2"	MB1218	Thorlabs	1
	?	Thorlabs	1
Ø 1.5" Damped Post, L = 8"	DP8A	Thorlabs	3
Ø 1.5" Mounting Post, 1/4"-20 Taps, L = 3"	P3	Thorlabs	2
	C1515	Thorlabs	1
USB DAQ			

Table 7.3: Parts List - Laser Path

	Description	Model/Part No.	Vendor	Qty.
Free Space	Polarized Coherent Laser (6W 532nm)	V6	Verdi	1
	Filter Wheel			1
	ND=? Filter			
	ND=? Filter			
	Mirror			1
	Linear Polarizing Filter			
	LC Polarization Rotator, 532nm	LCR1-532		1
	K-Cube LC Controller	KLC101	Thorlabs	1
Fiber Coupled	FiberPort Coupler			1

Table 7.4: Parts List - Illuminator Motion Assembly

	Description	Model/Part No.	Vendor	Qty.
Support Structure	Rotation Stage	RT-3	Newmark	1
	5 Series 20 hole - cross flat plate	4423-m ¹	80-20	1
	1.50" x 3.00" smooth extrusion	1530-S	80/20	1
	Sleeve bearing carriage	60585K76	McMaster-Carr	1
	Counterweight	SCTR-002	N/A	1
	Base plate	SCTR-003	N/A	1
	Variable Height P-Post	BLP01	Thorlabs	1
Illuminator Assembly	Ø1" Pillar Post, L=6"	RS6	Thorlabs	1
	SCTR-001-BasePlate	N/A		1
		SCTR-001-LeftSupport	N/A	1
		SCTR-001-RightSupport	N/A	1
		SCTR-001-InterfaceMount	N/A	1
		SCTR-001-BusMount	N/A	1
	Kinematic Mount for Ø1" Optic	KC1	Thorlabs	2
Homing Switch	Fiber Collimator (f=40mm FC/PC)	C40FC-A	Thorlabs	2
	Motorized Iris Diaphragm	ELL15	Thorlabs	2
	SM1 Coupler	SM1T2	Thorlabs	1
	Electrical Breadboard			1
	Translation Stage			

Table 7.5: Parts List - Counterweight

Table 7.6: Parts List - Sample Motion Assembly

Description	Model/Part No.	Vendor	Qty.
RT-3 Base Interface Plate	SCTR-004	N/A	1
RT-3 Stage Interface Plate	SCTR-005	N/A	1
Angle Bracket	56-666	Edmund Optics	1
Adapter Plate	RB13P1	Thorlabs	1
1" XYZ Translation Stage	PT3	Thorlabs	1

Table 7.7: Parts List - Acquisition Camera Assembly

Description	Model/Part No.	Vendor	Qty.
Camera		Point Grey	1
Lens Mount		Fotodiox	1
	XRR1	Thorlabs	1
	DP8A	Thorlabs	1
	BLP01	Thorlabs	1
	XT34SD-250	Thorlabs	1
	XT34C2	Thorlabs	2
	XT34D2-30	Thorlabs	2
	LMR3	Thorlabs	1
	SM3A95	Thorlabs	1
	SM3T2	Thorlabs	1
	PH1	Thorlabs	1
	TR075	Thorlabs	1
	XR25DR3	Thorlabs	1
	XR25DR2	Thorlabs	2

Table 7.8: Parts List - Sample Analysis Station

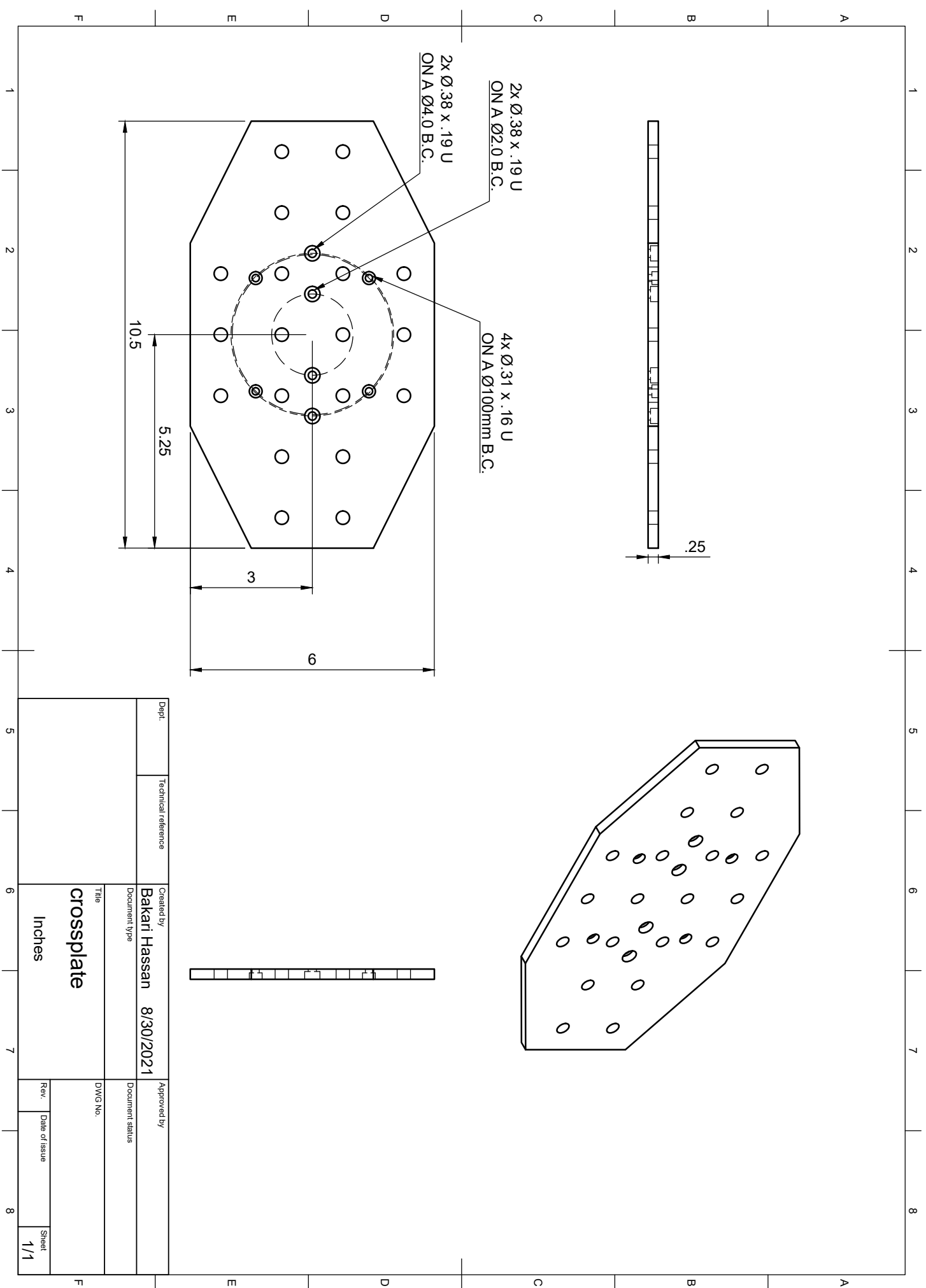
	Description	Model/Part No.	Vendor	Qty.
Optical Density Meter	Aluminum breadboard, 6" × 18" × 1/2"	MB618	Thorlabs	1
	Scientific camera	????	Point Grey	1
	Prime macro lens	AF-Micro 200mm f/4 D	Nikon	1
	40X Olympus achromat obective	RMS40X	Thorlabs	1
	EF-to-C lens mount	Nik-C	Fotodiox	1
	OD3 ND filter	NE30A	Thorlabs	1
	Ø1" pedestal pillar post	RS1P	Thorlabs	1
	One-axis 50mm translation mount	XF50	Thorlabs	1
	Ø1/2" post holder w/thumb screw	PH1	Thorlabs	2
	SM1-threaded 30mm cage plate	CP33	Thorlabs	2
Microscope	SM1 graduated ring iris diaphragm	SM1D12C	Thorlabs	1
	Collimated DPSS laser (532nm)	CPS532	Thorlabs	1
	Scientific camera	Prosilica GT3400	Allied Vision	1
	Prime macro lens	EF-Macro 180mm f/3.5 L	Canon	1
	EOS EF-to-C lens mount	EF-C	K&F Concept	1
	2-axis translation stage w/aperture	XYT1	Thorlabs	1
	2" pillar post (Ø1")	RS2	Thorlabs	1
	Ø1.25" pedestal base adapter	BE1	Thorlabs	1
	1" translation stage w/micrometer	PT1	Thorlabs	1
	Right-angle bracket	PT102	Thorlabs	1
2" post holder		03-655	Edmund Optics	2
Mounted LED (625nm, 700mW)		M625L3	Thorlabs	1
Brushed DC motor controller		KDC101	Thorlabs	1
DC actuator - 25mm travel		Z925B	Thorlabs	1

Table 7.9: Parts List - Sample Preparation & Analysis

Description	Model/Part No.	Vendor	Qty.
Dry block tube heater	30392080	Ohaus	1
Module block 20mm 8 wells	30400154	Ohaus	1
Module block 50mL, 15mL, 1.5mL	30400193	Ohaus	1
P1000L 100-1000µL pipette	FA10006M	Gilson	1
D1000 tip reload pack	F167014	Gilson	1
Microscope Slide (frosted)	N9302600	Perkin Elmer	1
Cover glass	CLS2980245	Corning	1
25µL gene frame	AB0576	Thermo Fisher	1
65µL gene frame	AB0577	Thermo Fisher	1
125µL gene frame	AB0578	Thermo Fisher	1
Milligram scale + boat	GEMINI-20-BLK	American Weigh Scales	1
Oval lab spoon	4916345	Scientific Labwares	1
Water squeeze bottle	CHWB 1020B	Eisco	1
IPA squeeze bottle	CHWB 1030	Eisco	1
Ethanol squeeze bottle	CHWB 1037	Eisco	1
Agarose, 50 G	A20090-50.0	RPI	1
Microscope	Custom ²	N/A	1
Optical density meter	Custom ³	N/A	1
4L HPLC water	W5-4	Fisher Chemical	1
Silica monodisperse 10µL spheres	904341-2G	Millipore Sigma	1
Kimwipes	34155	Kimtech	1
Nitrile gloves	MPR-50504	Med Pride	1
5µL centrifuge snap tubes	55105	SPL Life Sciences	1
15mL centrifuge snap tubes	50215	SPL Life Sciences	1
Microfiber towel	???		1

Chapter 8

Technical Drawings



Bibliography

- [1] Marina Alterman, Evgeniia Saiko, and Anat Levin. Direct acquisition of volumetric scattering phase function using speckle correlations. In *SIGGRAPH Asia 2022 Conference Papers*, pages 1–9, 2022.
- [2] Guillaume Bal. Inverse transport theory and applications. *Inverse Problems*, 25(5):053001, 2009.
- [3] Chen Bar, Marina Alterman, Ioannis Gkioulekas, and Anat Levin. A monte carlo framework for rendering speckle statistics in scattering media. *ACM Transactions on Graphics (TOG)*, 38(4):1–22, 2019.
- [4] Bruce J Berne and Robert Pecora. *Dynamic light scattering: with applications to chemistry, biology, and physics*. Courier Corporation, 2000.
- [5] R.D. Blevins. *Formulas for Dynamics, Acoustics and Vibration*. Wiley Online Library, 2015.
- [6] David A Boas, Dana H Brooks, Eric L Miller, Charles A DiMarzio, Misha Kilmer, Richard J Gaudette, and Quan Zhang. Imaging the body with diffuse optical tomography. *IEEE signal processing magazine*, 18(6):57–75, 2001.
- [7] Craig F Bohren and Donald R Huffman. *Absorption and scattering of light by small particles*. John Wiley & Sons, 2008.
- [8] Max Born and Emil Wolf. *Principles of optics: electromagnetic theory of propagation, interference and diffraction of light*. Elsevier, 2013.
- [9] Chengqian Che, Fujun Luan, Shuang Zhao, Kavita Bala, and Ioannis Gkioulekas. Towards learning-based inverse subsurface scattering. In *2020 IEEE International Conference on Computational Photography (ICCP)*, pages 1–12. IEEE, 2020.
- [10] William M Cornette and Joseph G Shanks. Physically reasonable analytic expression for the single-scattering phase function. *Applied optics*, 31(16):3152–3160, 1992.
- [11] Turgut Durduran, Regine Choe, Wesley B Baker, and Arjun G Yodh. Diffuse optics for tissue monitoring and tomography. *Reports on progress in physics*, 73(7):076701, 2010.

- [12] Philip Dutre, Philippe Bekaert, and Kavita Bala. *Advanced global illumination*. AK Peters/CRC Press, 2018.
- [13] Thomas J Farrell, Michael S Patterson, and Brian Wilson. A diffusion theory model of spatially resolved, steady-state diffuse reflectance for the noninvasive determination of tissue optical properties in vivo. *Medical physics*, 19(4):879–888, 1992.
- [14] Ronald Aylmer Fisher. Dispersion on a sphere. *Proceedings of the Royal Society of London. Series A. Mathematical and Physical Sciences*, 217(1130):295–305, 1953.
- [15] Jeppe Revall Frisvad, Niels Jørgen Christensen, and Henrik Wann Jensen. Computing the scattering properties of participating media using lorenz-mie theory. In *ACM SIGGRAPH 2007 papers*, pages 60–es. 2007.
- [16] Ioannis Gkioulekas, Anat Levin, and Todd Zickler. An evaluation of computational imaging techniques for heterogeneous inverse scattering. In *Computer Vision–ECCV 2016: 14th European Conference, Amsterdam, The Netherlands, October 11–14, 2016, Proceedings, Part III* 14, pages 685–701. Springer, 2016.
- [17] Ioannis Gkioulekas, Bei Xiao, Shuang Zhao, Edward H Adelson, Todd Zickler, and Kavita Bala. Understanding the role of phase function in translucent appearance. *ACM Transactions on graphics (TOG)*, 32(5):1–19, 2013.
- [18] Ioannis Gkioulekas, Shuang Zhao, Kavita Bala, Todd Zickler, and Anat Levin. Inverse volume rendering with material dictionaries. *ACM Transactions on Graphics (TOG)*, 32(6):1–13, 2013.
- [19] Kenji Hara, Ko Nishino, and Katsushi Ikeuchi. Mixture of spherical distributions for single-view relighting. *IEEE Transactions on Pattern Analysis and Machine Intelligence*, 30(1):25–35, 2007.
- [20] Louis George Henyey and Jesse L Greenstein. Diffuse radiation in the galaxy. *Annales d’Astrophysique*, Vol. 3, p. 117, 3:117, 1940.
- [21] C.Y. Ho, J.M. Holt, and H. Mindlin. *Structural Alloys Handbook: 1996 Edition; Incorporating Supplements Throught 1995*. Number v. 2. Cindas/Purdue Univ., 1997.
- [22] Hendrik Christoffel Hulst and Hendrik C van de Hulst. *Light scattering by small particles*. Courier Corporation, 1981.
- [23] Pramook Khungurn, Daniel Schroeder, Shuang Zhao, Kavita Bala, and Steve Marschner. Matching real fabrics with micro-appearance models. *ACM Trans. Graph.*, 35(1):1–1, 2015.

- [24] Matthew M Loper and Michael J Black. Opengl: An approximate differentiable renderer. In *Computer Vision–ECCV 2014: 13th European Conference, Zurich, Switzerland, September 6–12, 2014, Proceedings, Part VII* 13, pages 154–169. Springer, 2014.
- [25] William L Luyben. Simple method for tuning siso controllers in multivariable systems. *Industrial & Engineering Chemistry Process Design and Development*, 25(3):654–660, 1986.
- [26] Adolfo Munoz, Jose I Echevarria, Francisco J Seron, Jorge Lopez-Moreno, Mashhuda Glencross, and Diego Gutierrez. Bssrdf estimation from single images. In *Computer Graphics Forum*, volume 30, pages 455–464. Wiley Online Library, 2011.
- [27] Srinivasa G Narasimhan, Mohit Gupta, Craig Donner, Ravi Ramamoorthi, Shree K Nayar, and Henrik Wann Jensen. Acquiring scattering properties of participating media by dilution. In *ACM SIGGRAPH 2006 Papers*, pages 1003–1012. 2006.
- [28] Merlin Nimier-David, Sébastien Speierer, Benoît Ruiz, and Wenzel Jakob. Radiative backpropagation: An adjoint method for lightning-fast differentiable rendering. *ACM Transactions on Graphics (TOG)*, 39(4):146–1, 2020.
- [29] Merlin Nimier-David, Delio Vicini, Tizian Zeltner, and Wenzel Jakob. Mitsuba 2: A retargetable forward and inverse renderer. *ACM Transactions on Graphics (ToG)*, 38(6):1–17, 2019.
- [30] Jan Novák, Iliyan Georgiev, Johannes Hanika, and Wojciech Jarosz. Monte carlo methods for volumetric light transport simulation. In *Computer graphics forum*, volume 37, pages 551–576. Wiley Online Library, 2018.
- [31] Marios Papas, Christian Regg, Wojciech Jarosz, Bernd Bickel, Philip Jackson, Wojciech Matusik, Steve Marschner, and Markus Gross. Fabricating translucent materials using continuous pigment mixtures. *ACM Transactions on Graphics (TOG)*, 32(4):1–12, 2013.
- [32] Dave J Pine, Dave A Weitz, JX Zhu, and Eric Herbolzheimer. Diffusing-wave spectroscopy: dynamic light scattering in the multiple scattering limit. *Journal de Physique*, 51(18):2101–2127, 1990.
- [33] Lord Rayleigh. Xxxiv. on the transmission of light through an atmosphere containing small particles in suspension, and on the origin of the blue of the sky. *The London, Edinburgh, and Dublin Philosophical Magazine and Journal of Science*, 47(287):375–384, 1899.
- [34] LO Reynolds and NJ McCormick. Approximate two-parameter phase function for light scattering. *JOSA*, 70(10):1206–1212, 1980.

- [35] Denis Sumin, Tobias Rittig, Vahid Babaei, Thomas Nindel, Alexander Wilkie, Piotr Didyk, Bernd Bickel, J KRivánek, Karol Myszkowski, and Tim Weyrich. Geometry-aware scattering compensation for 3d printing. *ACM Transactions on Graphics*, 38(4), 2019.
- [36] Bertrand Thierry, Xavier Antoine, Chokri Chniti, and Hasan Alzubaidi. μ -diff: An open-source matlab toolbox for computing multiple scattering problems by disks. *Computer Physics Communications*, 192:348–362, 2015.
- [37] Jiajun Wu, Joshua B Tenenbaum, and Pushmeet Kohli. Neural scene de-rendering. In *Proceedings of the IEEE Conference on Computer Vision and Pattern Recognition*, pages 699–707, 2017.
- [38] Douglas R Wyman, Michael S Patterson, and Brian C Wilson. Similarity relations for the interaction parameters in radiation transport. *Applied optics*, 28(24):5243–5249, 1989.
- [39] Warren Clarence Young, Richard Gordon Budynas, Ali M Sadegh, et al. *Roark’s formulas for stress and strain*, volume 7. McGraw-hill New York, 2002.
- [40] Shuang Zhao, Ravi Ramamoorthi, and Kavita Bala. High-order similarity relations in radiative transfer. *ACM Transactions on Graphics (TOG)*, 33(4):1–12, 2014.
- [41] Quan Zheng, Gurprit Singh, and Hans-Peter Seidel. Neural relightable participating media rendering. *Advances in Neural Information Processing Systems*, 34:15203–15215, 2021.
- [42] John G Ziegler and Nathaniel B Nichols. Optimum settings for automatic controllers. *Transactions of the American society of mechanical engineers*, 64(8):759–765, 1942.